



**CHANGES TO TENSILE STRENGTH AND ELECTROMAGNETIC
SHIELDING EFFECTIVENESS IN NEUTRON IRRADIATED CARBON
NANOCOMPOSITES**

THESIS

James F. Shinn, Major, USA

AFIT-ENP-13-M-32

**DEPARTMENT OF THE AIR FORCE
AIR UNIVERSITY**

AIR FORCE INSTITUTE OF TECHNOLOGY

Wright-Patterson Air Force Base, Ohio

**DISTRIBUTION STATEMENT A.
APPROVED FOR PUBLIC RELEASE; DISTRIBUTION UNLIMITED.**

The views expressed in this thesis are those of the author and do not reflect the official policy or position of the United States Air Force, Department of Defense, or the United States Government.

**CHANGES TO TENSILE STRENGTH AND ELECTROMAGNETIC
SHIELDING EFFECTIVENESS IN NEUTRON IRRADIATED CARBON
NANOCOMPOSITES**

THESIS

Presented to the Faculty

Department of Engineering Physics

Graduate School of Engineering and Management

Air Force Institute of Technology

Air University

Air Education and Training Command

In Partial Fulfillment of the Requirements for the
Degree of Master of Science in Nuclear Engineering

James F. Shinn, BSE

Major, USA

March 2013

**DISTRIBUTION STATEMENT A.
APPROVED FOR PUBLIC RELEASE; DISTRIBUTION UNLIMITED.**

**CHANGES TO TENSILE STRENGTH AND ELECTROMAGNETIC
SHIELDING EFFECTIVENESS IN NEUTRON IRRADIATED CARBON
NANOCOMPOSITES**

James F. Shinn, BSE
Major, USA

Approved:

John W. McClory, PhD (Chairman)

Date

James Petrosky, PhD (Member)

Date

Shankar Mall, PhD (Member)

Date

Sarah A. Francis, PhD (Member)

Date

Abstract

Tensile strength and electromagnetic interference shielding effectiveness (EMI-SE) of nanocomposites containing multi-walled carbon nanotubes (MWNTs) arranged as two plies of MWNTs in an epoxy resin, and 4 plies of an E-glass substrate, were investigated following neutron irradiation. EMI-SE measurements over the X-band frequency spectrum and monotonic tension tests to determine Young's Modulus were performed before and after irradiation of the nanocomposite materials to 1.5×10^{14} n/cm² 1 MeV (Si-eq) neutrons. The tensile strength and Young's Modulus had a 6% and 10% increase, respectively, following irradiation. This increase, while not significant, is likely a result of the neutron-induced embrittlement of the polymer matrix.

The nanocomposites had an average increase of 6 dB, or 400%, in shielding effectiveness after irradiation. However, the increase was not permanent, with a return to pre-irradiation values after approximately 10 days at room temperature and standard atmospheric pressure. The initial EMI-SE increase is dominated by damage-induced cross-linking in the polymer chains. The impermanence of the increase in the EMI-SE is likely due to annealing in these polymer chains over time.

Raman spectra of the MWNT plies had a D/G peak ratio increase from 0.19 to 0.49, or 150%, after irradiation. This indicates damage in the plies due to neutron interactions in the MWNTs that does not lead to a commensurate reduction in EMI-SE or tensile strength in the nanocomposite material.

Acknowledgments

I would like to thank the organizations and people listed below. Their expertise and assistance was instrumental in completing this research.

James F. Shinn

Air Force Research Laboratory – Materials Directorate

Dr. Max Alexander

Ben Wilson

Air Force Research Laboratory – Sensors Directorate

Dr. Elizabeth Moore

John Hoelscher

Capt. Merle Hamilton, USAF

Air Force Institute of Technology – Engineering Physics Department

Dr. Volodymyr Sabelkin

Dr. Alex Li

Barry Page

Greg Smith

AFIT Model and Fabrication shop

Table of Contents

	Page
Abstract	iv
Acknowledgments.....	v
Table of Contents	vi
List of Figures	viii
List of Tables	xiv
I. Introduction	1
1.1 Objective of Research	3
II. Background	5
2.1 Challenges of the Space Environment	5
2.2 Composite Material	8
2.3 Carbon Nanotubes	9
2.4 The Sample Material	13
2.5 Results of Previous Work	14
III. Theory	16
3.1 Electromagnetic Interference Shielding Effectiveness	16
3.2 Mechanical Properties	19
3.3 Raman Spectroscopy	22
3.4 Raman Spectroscopy in Carbon Nanotubes	23
3.5 Neutron Interactions.....	26
3.6 Neutron Interactions in CNTs	28
IV. Methodology.....	30
4.1 Sample Preparation	30
4.2 Sample Irradiation	30
4.3 Mechanical Measurements.....	33
4.4 EMI-SE Measurements	37
4.5 Raman Spectroscopy	40
V. Results and Analysis	43
5.1 Mechanical Measurements.....	43
5.2 EMI-SE	47

5.3 Raman Spectroscopy	56
VI. Conclusions and Recommendations	64
6.1 Conclusions	64
6.2 Recommendations for Future Research	67
Appendix A.....	70
BIBLIOGRAPHY	72

List of Figures

	Page
Figure 1. Diagram showing the Van Allen radiation belts [8].....	7
Figure 2. Example of SWNT (on the left) and MWNT (on the right) [14].	10
Figure 3. Diagram of the chiral angles of carbon nanotubes.	12
Figure 4. Planar diagram of a graphene sheet showing the different types of CNT chirality based on the angle of the roll of the sheet [18].	12
Figure 5. The image on the left is an optical microscope photo taken at $22\times$ magnification. The image shows the MWNT plies (top black), 4 layers of woven E- glass (light yellow), and the epoxy resin, BMI, used in making the composite. On the right is a schematic of the nanocomposite being studied. There are two plies of MWNTs on a substrate made of 4 plies of E-glass, with the resin layer being included in with the E-glass.....	13
Figure 6. Plane wave incident on a slab of finite thickness of shielding material with multiple internal reflections.	17
Figure 7. Sample stress-strain curves for brittle materials (left) and ductile materials (right). Note that on the brittle curve, the ultimate tensile strength (2) is the point of fracture. On the ductile curve, the highest stress is at (1) and the fracture stress is at (4), which is less than ultimate tensile strength [25].	20
Figure 8. This plot shows the linear region of the stress-strain curve. This region is where Young's Modulus, or E, is determined by calculating the slope using two points on the linear portion of the curve.	22

Figure 9. Example of a Raman spectrum for a SWNT thin film sample [29]. The radial breathing mode (RBM) peak is shown at the far left. The D and G peaks are shown at 1351 and 1596 cm^{-1} , respectively.	24
Figure 10. An example of two Frenkel defects within the NaCl structure. The empty boxes represent locations where the Na atoms were dislocated and the red circles with boxes around them represent the interstitial locations where they reattached to the structure [33].	29
Figure 11. The image on the left shows cross-linking externally between different SWNTs. The image on the right shows cross-linking internally between concentric tubes in an MWNT. In MWNTs, cross-linking occurs internally and externally from MWNT to MWNT. Reproduced with permission from Krashenikov, <i>et al.</i> [34].	29
Figure 12. This figure shows the samples on the plexiglas holder with the samples wired to the holder using 0.3" diameter aluminum wire.	31
Figure 13. The OSURR as viewed from above looking into the cooling pool at the reactor. The dry tube is marked on the left and the reactor control rod tubes are also marked. The reactor is at the bottom of the pool.	32
Figure 14. This figure shows the sample holder with the mounted samples being placed into the cadmium box mounted on the apparatus. The rope shown on the left side of the apparatus is used to lower the entire setup into the dry tube chamber.	33
Figure 15. The upper sample shows the red tabs that have been attached to the sample for testing, as compared to the lower sample that has yet to be prepared.	35
Figure 16. The sample mounted in the MTS 810 ready to begin the monotonic tension test.	37

Figure 17. The fixture on the left is the waveguide used for sample mounting for network analyzer measurements. On the right is the shielding block used in calibration, and on the bottom left is a sample.	38
Figure 18. Photograph showing a sample being secured into the Agilent Technologies E8362B PNA Series Microwave Network Analyzer. The waveguide is secured by hex cap screws and nuts tightened to the torque specifications of the Agilent Technologies 0.9 N-m torque wrench. The left side is the port adaptor for port 1, and port 2 is on the right side of the photo.	39
Figure 19. Photograph of the EMI-SE oriented face (MWNT ply) down. The five samples on the left are the samples that were neutron-irradiated. Sample 4 on the right was added to show the color change caused by irradiation. The numbers and arrow indicators are also visible.	40
Figure 20. This image shows an example of the circular map made for the Raman study. The circle represents a 3 mm diameter with spectra recorded at 100 micron intervals for a total of 2496 data sets. In this example, the color represents the G peak intensity of the MWNT ply sample for the pre-irradiation measurement.	42
Figure 21. The average stress vs. strain curve for the pre- and post-irradiation samples. The pre-irradiation curve is in red and the post-irradiation curve is in blue.	44
Figure 22. Photograph showing all of the samples tested to failure except for sample 16. The tabs on the bottom of sample 16 failed to remain adhered to the sample, and when the sample slipped out, it was not tested to failure. Sample 9 is unique to the sample set in that it failed in two locations simultaneously.	47

Figure 23. Images taken from an optical microscope. The image on the left is at (50× magnification) and shows the edge of the MWNT ply. The image on the right is at (10× magnification), and is a close up of one fiber bundle showing the fracture of the E-glass.....	47
Figure 24. The EMI-SE measurements for sample 7 at four different time intervals relative to neutron irradiation. The time intervals are: Pre-Irradiation, 96 hours post-irradiation, 216 hours post-irradiation, and 264 hours post-irradiation.....	48
Figure 25. The EMI-SE measurements for sample 8 at four different time intervals relative to neutron irradiation. The time intervals are: Pre-irradiation, 96 hours post-irradiation, 216 hours post-irradiation, and 264 hours post-irradiation.....	49
Figure 26. The EMI-SE measurements for sample 9 at four different time intervals relative to neutron irradiation. The time intervals are: Pre-irradiation, 96 hours post-irradiation, 216 hours post-irradiation, and 264 hours post-irradiation.....	50
Figure 27. The EMI-SE measurements for sample 10 at four different time intervals relative to neutron irradiation. The time intervals are: Pre-Irradiation, 96 hours post-irradiation, 216 hours post-irradiation, and 264 hours post-irradiation.....	51
Figure 28. The EMI-SE measurements for sample 11 at four different time intervals relative to neutron irradiation. The time intervals are: Pre-Irradiation, 96 hours post-irradiation, 216 hours post-irradiation, and 264 hours post-irradiation.....	52
Figure 29. Average EMI-SE results plotted by time interval. In sequential order, the blue curve represents the pre-irradiation measurement, the green curve represents 96 hours post-irradiation, the red curve represents 216 hours post-irradiation, and the magenta curve represents 264 hours post-irradiation.	54

Figure 30. Front walls of one and the same SWNT just after impact (a) and annealing (b).

During annealing, the double vacancy (D) and the single vacancy (S) are transformed into non-hexagonal rings. Reproduced with permission from Krashenikov, *et al.*

[34]..... 55

Figure 31. A side view of a MWNT before (left) and after (right) irradiation. The right hand image shows the cross-linking that can occur in the MWNT as atoms are

displaced. Rather than fill vacancies along the tube it was displaced from, it can

bond across tubes, cross-linking them together. Reproduced with permission from

Krashenikov, *et al.* [34]. 56

Figure 32: The Raman spectra of the MWNT ply sample with normalized intensity. The

red curve represents the pre-irradiation spectrum and the black curve represents the

post-irradiation spectrum. Of note is the large increase in the D-peak due to neutron

induced damage of the MWNTs during irradiation..... 57

Figure 33. Normalized D/G ratio for the pre-irradiation MWNT ply sample. The color

scale on the right represents intensity (arbitrary units) of the D/G ratio. The sample

appears mostly black, which is a visual depiction of the calculated average D/G ratio

of 0.19 ± 0.04 58

Figure 34. Normalized D/G ratio for the post-irradiation MWNT ply sample. The color

scale on the right represents intensity (arbitrary units) of the D/G ratio. The sample

appears mostly green, which is a visual depiction of the calculated average D/G ratio

of 0.48 ± 0.11 59

Figure 35. A single point Raman spectra of the nanocomposite sample with normalized

intensity. The red curve represents the pre-irradiation spectrum and the black curve

represents the post- irradiation spectrum. Of note is the small increase,
approximately 0.05 (arb. units), in the D-peak due to neutron damage of the MWNTs
during irradiation. 61

Figure 36. Single point Raman spectra of the pre- and post-irradiated nanocomposite
sample. The focus of this spectra is to show the change in the D'-peak before and
after irradiation. 63

Figure 37. The Raman spectra of the nanocomposite sample. The red curve represents
the pre-irradiation spectra and the black curve represents the post irradiation curve.
There appears to be a large change caused by radiation, but the intensities are not
normalized. 70

Figure 39. The Raman spectra of the nanocomposite sample. The red curve represents
the pre-irradiation spectra and the black curve represents the post irradiation curve.
The peak intensities have been normalized and the data now appears to be
inconclusive. 71

List of Tables

	Page
Table 1. Baseline standards for proton fluxes of LEO satellites and electron fluxes of GEO satellites.	8
Table 2. The average tensile strength and Young's Modulus for the pre- and post- irradiation measurements.	45
Table 3. Mean EMI-SE by sample at each tested interval.	53

CHANGES TO TENSILE STRENGTH AND ELECTROMAGNETIC SHIELDING EFFECTIVENESS IN NEUTRON IRRADIATED CARBON NANOCOMPOSITES

I. Introduction

Space exploration began in 1942 when the Germans launched the first manmade object, a V-2 rocket, into space. The human race has been exploring space ever since, but we have much more exploration to conduct. Today the most common space mission efforts focus: communications, remote sensing, navigation, or science and exploration [1]. These missions are conducted for both national defense and commercial applications.

Students of history can easily trace the importance of the “high ground” as warfare has evolved. Space offers a global perspective; therefore it is the ultimate high ground and naturally has implications for national defense [1]. The United States military’s push for enhanced C4ISR (command, control, communications, computers, intelligence, surveillance and reconnaissance) requires that advanced systems be deployed in orbit around the world. In addition, commercial use of space has greatly enhanced everyday lives. Global Positioning Systems (GPS) used for navigation, satellite television, and satellite communications are all dependent on satellites.

The need to continue using space-borne vehicles for military or civilian purposes is evident. With costs ranging from \$2,000 to \$10,000 per pound to launch an object into space, reducing the structural mass of a spacecraft can potentially save hundreds of thousands of dollars in launch costs [1]. One way of reducing the mass is to use composite materials in place of denser materials such as aluminum when possible.

Current high performance composite technology has reduced the structural weight to approximately 6 – 8% of the spacecraft's total dry weight [2]. In addition to weight savings, the materials used to build these systems need to be mechanically strong enough to maintain integrity during launch as well as operations in space.

In addition to the weight/cost savings, the use of new composite materials may also provide better protection to the satellite from the space environment. By designing composite materials to have tailored properties, it is possible to construct a smaller and lighter structure that provides better protection to objects within space craft. Materials can be designed to maximize the mechanical strength needed for structural integrity while also maintaining a high conductivity to allow for higher electromagnetic interference shielding effectiveness (EMI-SE). High conductivity also allows the structure to electrically equilibrate and prevent flashover and internal electromagnetic pulse (IEMP) in space caused by non-uniform charge build up in orbit.

Recent advances in nanocomposites offer the technology to meet these challenges. Several companies are producing composite materials in a variety of configurations that potentially meet these requirements of spacecraft. Before a material can be selected, however, it must be thoroughly tested. Experiments testing a material's ability to perform in a simulated space environment have been conducted at the Air Force Institute of Technology (AFIT) recently [3], [4], [5], [6]. These experiments were designed to test mechanical and electrical properties of composites before and after exposure to radiation, similar to that found in the space environment. The tests range from tensile strength to electrical conductivity of the material, and have been performed on numerous varieties of nanocomposites. Previous research has been similar in methods

and scope. Total fluences used for electron and neutron irradiations have been selected based on an estimated dose received by a satellite through its operational lifetime. These experiments have validated that the materials studied meet or exceed standards required for a material to be used in space as established in Military Standard-1809 (MIL-STD-1809), the standard for the space environment for USAF space vehicles. The approach of this research will be to test similar properties of a nanocomposite material using a higher fluence of radiation in order to produce measureable damage to the material. By producing a large damage differential, the effects of the radiation can be more easily observed.

1.1 Objective of Research

The purpose of this work is to investigate the effects of neutron irradiation on the mechanical and electrical properties of a multi-walled carbon nanotube (MWNT) nanocomposite to determine its validity for use in space applications. Specifically, the tensile strength (TS) and Young's Modulus (E), as well as electromagnetic interference – shielding effectiveness (EMI-SE) will be measured pre- and post-neutron irradiation. Raman spectroscopy will be used to delineate the radiation damage to the MWNTs or in the polymer. The primary objectives of this work are:

1. Establish EMI-SE and monotonic tension test methods in accordance with IEEE, Military Standard (MIL-STD), and American Society for Testing Materials (ASTM).
2. Experimentally measure the effect of neutron irradiation on the mechanical and electrical properties of MWNT nanocomposites.

3. Attribute results to the interaction of neutron irradiation with MWNTs or polymer. If feasible, quantify the radiation damage to the MWNTs and the polymer.

A literature review found that neutron radiation is expected to cause displacement damage to the MWNT plies and the polymer used in the epoxy resin forming the composite. Based on the results of previous research [3], [6], it is expected that there will be an increase in conductivity following neutron irradiation. The increase in conductivity will result in an increase in EMI-SE effectiveness, but may not be permanent. As shown in [3], after several days at room temperature and ambient pressure, the EMI-SE signal returned to the pre-irradiation values in EMI-SE.

Neutron irradiation is known to cause embrittlement in materials, which should increase the Young's Modulus. Damage to the lattice structure of the MWNT plies should reduce the tensile strength of the nanotube layers, but the overall strength of the composite studied is believed to be provided by the E-glass substrate. Neutron displacement is also believed to lead to shortening of the polymer chains used as the matrix in the composite. This shortening of the polymer chains is believed to result in a reduction in tensile strength of the composite.

II. Background

Chapter Overview

This chapter describes the basic environment experienced by a spacecraft which must be accounted for in its design. Composite materials are explained and an overview of MWNTs is provided. This chapter ends with an introduction to the specific nanocomposite studied in this research.

2.1 Challenges of the Space Environment

The nanocomposite to be studied is being considered for use in space applications, so it is imperative that the space environment be considered. There are three major sources of radiation in the geo-local space environment: galactic cosmic rays (GCR), solar proton events (SPE), and the Van Allen radiation belts. GCRs are high energy charged particles that originate inside our galaxy, but outside of our solar system. They potentially cause dense ionization tracks as they pass through matter [2]. SPEs occur when protons emitted by the sun become accelerated to high energies either close to the sun during a solar flare, or in interplanetary space by shocks associated with coronal mass injections. They temporarily enhance the radiation in the space around the earth's magnetosphere and may penetrate to low altitudes in the polar region. Energetic solar protons are a significant radiation hazard to spacecraft and astronauts, which can receive large amounts of absorbed dose from the ionizing radiation.

The amount of long term radiation received by a satellite is greatly dependent upon its location with respect to the sun, the earth's magnetosphere, the level of solar activity during its orbit, and the cross-sectional area of the platform exposed to the

radiation stream [2]. The majority of satellites operate in low earth and geostationary orbits (LEO/GEO), ranging in altitude from 200-35,000 kilometers above the earth's surface. Satellites in GEO circle the earth at approximately 35,000 kilometers above the earth while satellites in LEO circle the earth at approximately 2000 kilometers above the earth. Both orbits result in satellite interaction with the Van Allen radiation belt.

The Van Allen radiation belt is comprised of two layers, or "belts" of energetic charged particles (plasma) around the planet due to the earth's magnetic field. The outer belt ranges from 13,000-60,000 kilometers above the earth's surface. The trapped particles in the outer belt vary, but they are primarily high energy electrons (10-100 MeV) and various ions which are mostly energetic protons, with a small percentage of alpha particles and O^+ ions. The inner belt is located 500-13,000 km above the earth's surface and contains mostly protons of energy greater than 10 MeV, and also low energy electrons below 10 MeV [7].

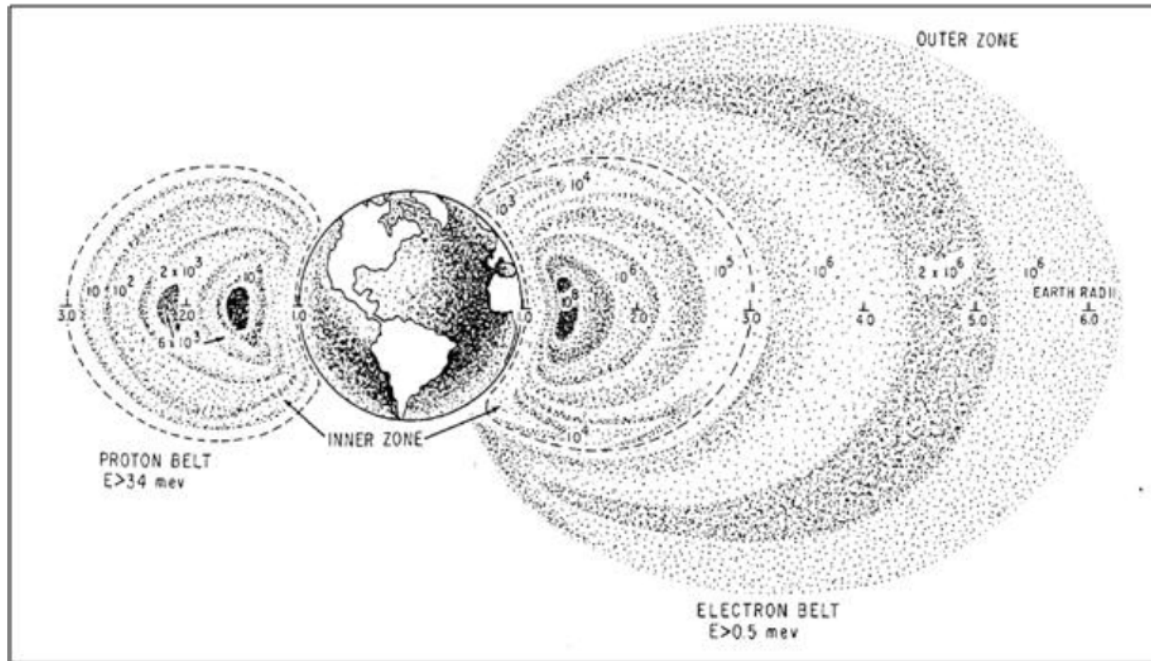


Figure 1. Diagram showing the Van Allen radiation belts [8].

High energy electrons can damage the electronic components of a satellite and render it inoperable. The electrons generally do not contribute to surface charging effects as they penetrate the surface materials. As such, low energy electrons, below 10 MeV, are primarily responsible for surface charging and associated electrostatic discharge (ESD) [7].

For the purpose of space operation validation and evaluation, the space radiation environment is defined by MIL-STD-1809, which also gives flux values for proton and electron radiation at various altitudes. The values provided in Table 1 are the parameters for which components must be validated against to meet military specifications.

Table 1. Baseline standards for proton fluxes of LEO satellites and electron fluxes of GEO satellites [7].

Proton Energy (MeV)	Flux (protons cm⁻² sec⁻¹)
> 0.1	4×10^7
> 1	1×10^7
> 10	5×10^5
> 100	2×10^4
> 400	8×10^2
Electron Energy (MeV)	Flux (electrons cm⁻² sec⁻¹)
> 0.1	2×10^7
> 0.5	8×10^6
> 1	2×10^6
> 2	2×10^4

2.2 Composite Material

Composites are materials that are made up of multiple individual, or constituent, materials. Constituents are segregated into two categories: matrix and reinforcement. It is common for the reinforcement to be referred to as the fiber. Many times, the matrix is an epoxy resin, or polyimide, generally referred to as the resin or polymer. At least one of each is required to make a composite, but multiple materials from each category may be used. A nanocomposite is defined as a multiphase solid material where one or more of the phases have at least one dimension of less than 100 nanometers.

The matrix material surrounds the reinforcement material, and the bond formed between the matrix and fiber keeps the reinforcements in their relative positions. The reinforcement imparts its mechanical and physical properties to enhance the matrix properties. The combination of the two constituents produces bulk properties unavailable from the individual constituent materials. An example of a composite is concrete – cement (matrix) and aggregate, or gravel, (reinforcement), and sometimes rebar (reinforcement).

An important property of composites is the interface between the fiber and the matrix. Short-fiber composites are more sensitive to interface effects because there is relatively little interface per fiber for the transfer of stress [9]. This applies to short fiber composites, as well as long fiber composites whose polymer chains are broken by damage such that they exhibit the characteristics of short fiber polymers. A common thermosetting epoxy resin is bismaleimide. This polymer offers improved high-temperature properties relative to the epoxy system and improved processability relative to the linear high-molecular-weight polyimides [9]. The most serious disadvantage of bismaleimide systems is their extreme brittleness. Techniques to increase the toughness mainly include increasing the chain length between the terminal maleimide groups (decreasing the cross-link density) and the addition of toughening plastics [9].

2.3 Carbon Nanotubes

A large percentage of academic and popular literature attributes the discovery of the carbon nanotube to Sumio Iijima of the Nippon Electric Company, or NEC, in 1991 [10]. Carbon nanotubes (CNTs) are allotropes of carbon with a cylindrical nanostructure

that have unusual properties, making them valuable for nanotechnology, electronics, optics, and materials science. Thermal conductivity, as well as mechanical and electrical properties, makes CNTs a valuable additive to structural materials as they are able to enhance these characteristics to meet design needs [11].

A CNT made of a single graphene layer rolled up into a hollow cylinder is called a single-walled nanotube (SWNT). A tube comprised of several concentrically arranged cylinders is referred to as a multi-walled nanotube (MWNT). Examples of SWNT and MWNT are shown in Figure 2. MWNTs have similar lengths as SWNTs (microns), but much larger diameters, measuring around 5 and 100 nm, for the inner and outer diameters, respectively [12]. Structurally, CNTs are the stiffest materials yet discovered in terms of tensile strength and elastic modulus [13]. This strength results from the covalent sp^2 bonds formed between the individual carbon atoms.

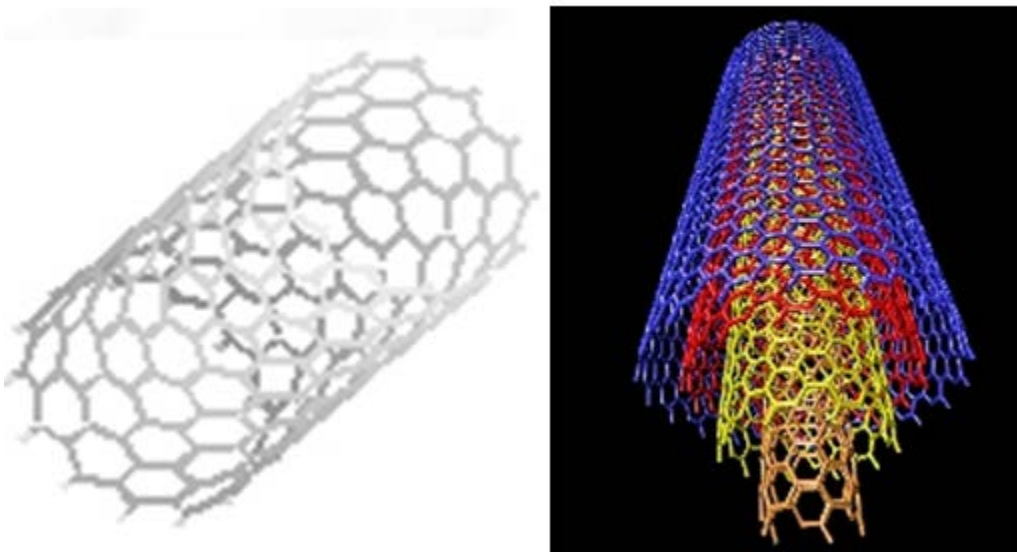


Figure 2. Example of SWNT (on the left) and MWNT (on the right) [14].

The sheets of graphene can be rolled at specific chiral angles, which is the primary method of obtaining the specific properties of each. The different chiralities are armchair, zigzag, and chiral, as shown in Figure 3 and Figure 4. In terms of electrical characteristics, the armchair chirality is metallic, and the zigzag chirality can be either metallic or semiconducting based on the specific chiral vector, C_h , specified by

$$C_h = na_1 + ma_2, \quad (1)$$

which is often described by a pair of indices (n,m) that denote the number of unit vectors na_1 and ma_2 in the hexagonal honeycomb lattice containing C_h [15]. When $(2n) + m$ is an integer multiple of three, the CNT is metallic in behavior, and all others are semiconducting in nature. The chiral CNTs have no specific chiral vector other than not being armchair or zigzag, and are semiconducting in characteristic. The chirality also affects mechanical properties, such as tensile strength and modulus of elasticity. For individual nanotubes, the armchair variety has the highest tensile strength and roughly the same elastic modulus as the zigzag variant [16].

Testing has shown that as little as 1 percent (weight) of MWNTs added to a composite can substantially enhance the EM wave absorption of the material [17]. This can be further enhanced by filling the MWNTs with metals such as Fe or Ni. The enhancement is due to the conductive nature of the MWNTs. The effect of conductivity on EMI-SE will be discussed in more detail in the EMI-SE theory section of this work.

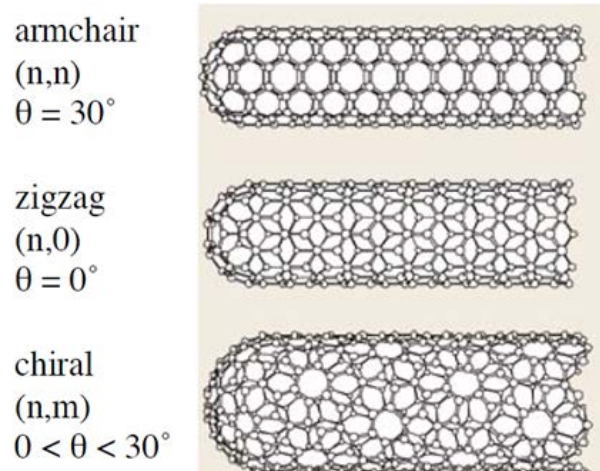


Figure 3. Diagram of the chiral angles of carbon nanotubes.

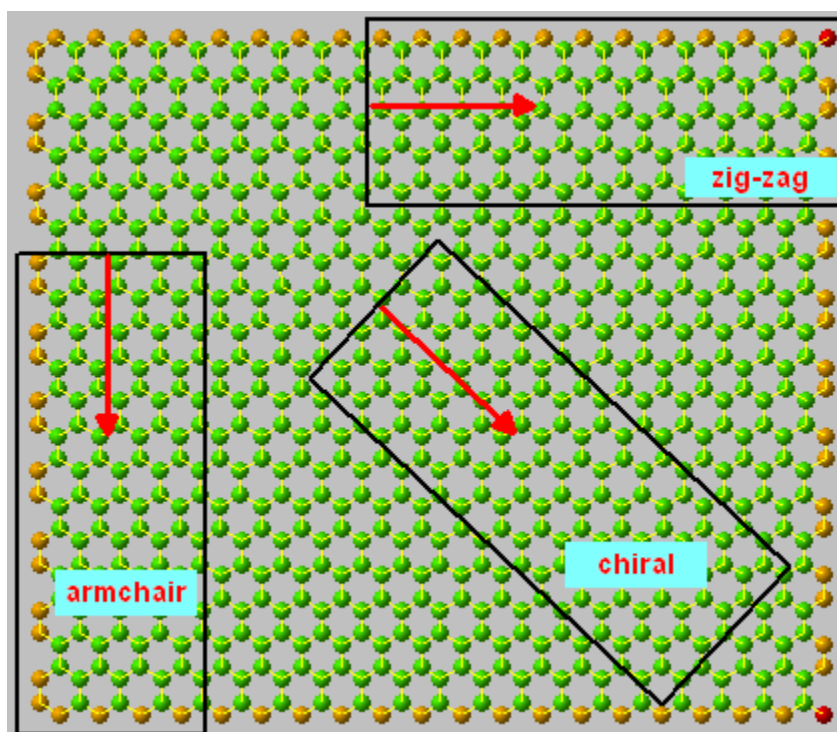


Figure 4. Planar diagram of a graphene sheet showing the different types of CNT chirality based on the angle of the roll of the sheet [18].

2.4 The Sample Material

The material studied is a nanocomposite produced by Northrup Grumman in conjunction with the Air Force Research Laboratory (AFRL). The MWNT plies used were fabricated by Nanocomp Technologies, Inc. (NCTI) located in Concord, New Hampshire. The ply is a thin sheet made from a macroscopic aggregate of CNTs. It is a convenient method of handling the CNTs and a thin sheet, or ply, makes it a good choice to use in composites. The plies were fabricated by chemical vapor deposition and have a density of approximately 11 grams per square meter while the fiber content, MWNTs, is 50 percent by volume. The fiberglass used as a substrate was a woven E-glass peel ply made by Cytec. The nanocomposite consists of two MWNT plies infused in a resin, bismaleimide (BMI), pressed onto four layers of E-glass and BMI as shown Figure 5.

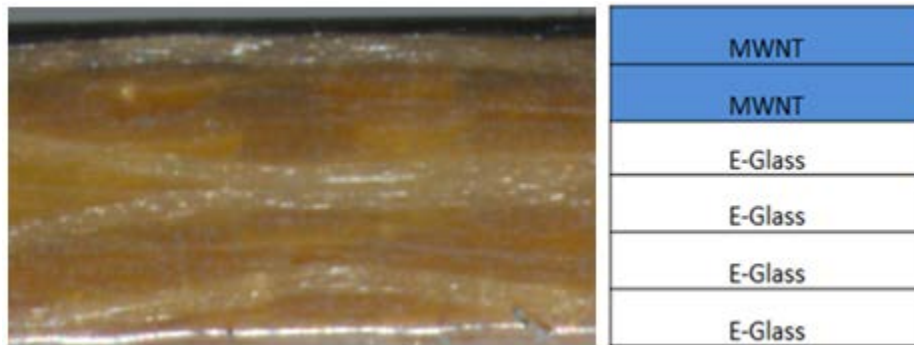


Figure 5. The image on the left is an optical microscope photo taken at $22\times$ magnification. The image shows the MWNT plies (top black), 4 layers of woven E-glass (light yellow), and the epoxy resin, BMI, used in making the composite. On the right is a schematic of the nanocomposite being studied. There are two plies of MWNTs on a substrate made of 4 plies of E-glass, with the resin layer being included in with the E-glass.

2.5 Results of Previous Work

This study follows research performed on similar composite materials at the Air Force Institute of Technology. In 2009, McGary [19] studied the electrostatic discharge properties of irradiated nanocomposites. Seven different configurations of nickel nano strand composites were studied before and after electron irradiation. The samples were irradiated at a fluence of 10^{16} e⁻/cm² at an average energy of 500 keV. The research found no common response between the electrical performance based on location or density of nickel nano-strands in the material [19]. The surface resistivity increased in each configuration following irradiation, while the change in bulk resistivity was correlated to the type of epoxy used in the composite. The increase in surface resistivity indicates a decrease in the EMI-SE of the material due to the relationship of conductivity and shielding effectiveness. This will be discussed later in the theory section of this paper.

In 2010, Coy studied changes to electrical conductivity in irradiated carbon-nickel nanotubes [20]. Resistivity measurements were made before and after electron irradiation to a total fluence of 4×10^{16} e⁻/cm² at an average energy of 500 keV [20]. The results of this research show a 14-30% decrease in surface resistivity following irradiation. The results were determined to be consistent with other research conducted on composites utilizing similar epoxy types. The decrease in resistivity results in increased conductivity, which in turn increased EMI-SE.

In 2011, Duncan studied the changes to electrical conductivity in irradiated carbon nanocomposites [6]. This research compared the properties of CNT composites with the properties of carbon nanofiber (CNF), composites. Both have low resistivity,

but the CNTs were found to be substantially more conductive [6]. The samples were subjected to electron irradiation to a fluence of 10^{16} e⁻/cm² at an average energy of 500 keV and neutron irradiation to a fluence of 10^{14} n/cm² at 1 MeV Si equivalent. There were no observed changes in the resistivity of the CNF sample, but there was a 4% and 26% increase in the resistivity of the CNT samples following neutron and electron irradiation, respectively. The increases indicate a decrease in EMI-SE. The CNT composite resistivity recovered to the pre-irradiation values after 240 hours at ambient temperature and pressure.

In 2012, Lu studied the durability of MWNT composites under electron and neutron irradiation [3]. Two sets of samples were studied, one for each type of irradiation. The samples consisted of three configurations of composites, as well as a control sample. One set was irradiated to a fluence of 10^{16} e⁻/cm² at an average energy of 500 keV. These samples showed an increase in EMI-SE and conductivity following the electron irradiation. The increased values both returned to the pre-irradiation values after days at ambient temperature and pressure. Following neutron irradiation to fluences up to 10^{15} n/cm², only minor changes were observed in conductivity and no change was observed in EMI-SE.

III. Theory

Chapter Overview

This chapter provides a general background into the theory governing this research. The theory covers EMI-SE, tensile testing, and Raman spectroscopy. The mechanisms of neutron interactions in matter are also discussed.

3.1 Electromagnetic Interference Shielding Effectiveness

There are two methods used to approach the theory of electromagnetic interference shielding: circuit theory and wave theory. The circuit theory approach uses mathematical modeling techniques to predict field strength at any given distance from the shielding barrier material. The electromagnetic compatibility (EMC) industry uses a wave theory approach to shielding theory, which uses abstract mathematical modeling techniques to yield a value of merit classified as “shielding effectiveness”. Shielding effectiveness is then used as a measurement to gauge the attenuation of the electromagnetic fields through shielding barrier material [21].

For the purpose of this research, the wave theory was selected because it represents the method used by the equipment available to measure EMI-SE. Shielding is accomplished 1 of 2 ways: 1) shielding internal components from outside sources of EMI, and 2) shielding external components from EMI emitted from sources internal to the shielding. This research focuses on shielding the internal electronics package from the external EMI sources encountered in the space environment.

A far field EM wave incident on a slab of finite thickness will be used as the model for shielding in the present work. For far field radiation, the incident wave will

resemble a uniform plane wave. The most general case, as shown in Figure 6, occurs when an incident wave strikes the surface of the shielding material, or slab, which has different intrinsic impedance than the medium surrounding the shield. The initial wave, E_{inc} , can be reflected or transmitted into the shielding material [22]. When the wave transmitted into the slab of material reaches the interface on the far side of the material, it can reflect, transmit, or both. If there is another reflection, called a multiple reflection, the wave will continue to attenuate in the material. The result of the reflections is to reduce, or attenuate, E_{inc} as it passes through the material.

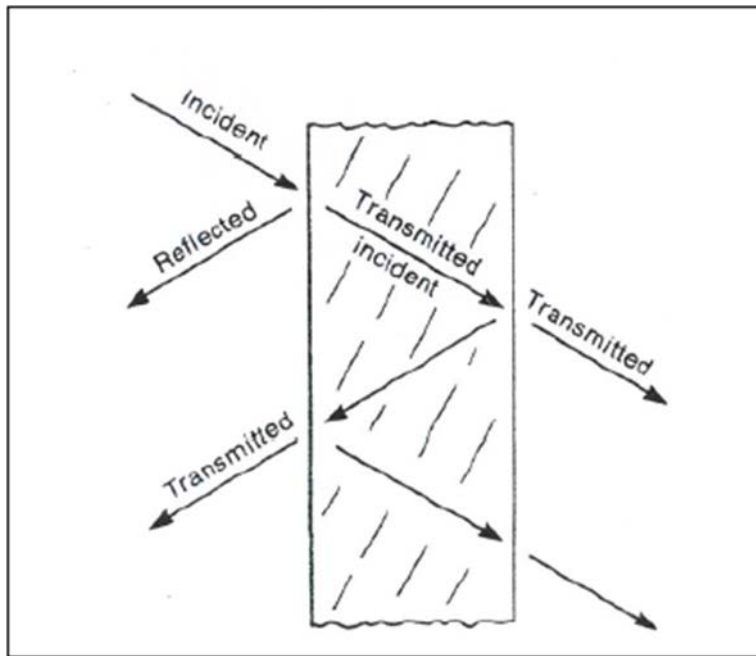


Figure 6. Plane wave incident on a slab of finite thickness of shielding material with multiple internal reflections.

The most basic expression for the total shielding effectiveness (SE) is

$$SE_{db} = R_{db} + A_{db} + M_{db} \quad (2)$$

where R is the power loss due to reflection, A is the power loss due to absorption, and M is the power loss due to multiple reflections [23]. The subscript $_{db}$ indicates that power loss is in decibels. The relationships for R , A , and M are given by equations (3)-(5).

$$R_{db} = 20 \log_{10} \left| \frac{\eta_0}{4\eta_m} \right| \quad (3)$$

$$A_{db} = -20 \log_{10} \left| e^{\frac{t}{\delta}} \right| \quad (4)$$

$$M_{db} = -20 \log_{10} \left| 1 - e^{\frac{t}{\delta}} \right| \quad (5)$$

In equation (3)-(5), η_0 and η_m are the intrinsic impedance of free space and the intrinsic impedance of the shielding material, respectively, t is the thickness of the shielding material, and δ is the skin depth of the material [23]. Skin depth is defined as the distance through a shielding material that it takes to reduce the amplitude of the incident wave by a factor of $1/e$. Skin depth can be approximated using

$$\delta = \sqrt{\frac{2}{\omega \mu \sigma}} \quad (6)$$

where μ is the magnetic permeability of the material, σ is the conductivity of the material, and ω is the frequency of the incident wave.

From Equation (6), there is a direct relationship between skin depth and conductivity. Materials with higher conductivity have shorter skin depths. Since the skin depth is a function of the material, it will not change as the material thickness changes.

When t is much greater than δ , the shielding effectiveness is high. When t is much lower than δ , the shielding effectiveness is low.

One method of increasing the ratio of t to δ is to increase the conductivity of the material. Conductivity of a composite material can be changed by using different fillers. MWNTs have been shown to greatly increase the conductivity of composite materials. Since the MWNTs enhance conductivity, they will also increase EMI-SE.

3.2 Mechanical Properties

Samples of engineering materials are subjected to a wide variety of mechanical tests to measure their strength or other properties of interest. The samples are usually broken or permanently deformed because they are often tested to failure. The most basic test is one in which the sample is broken by applying a tensile force to each end and pulling until the sample breaks. Compression tests and various bending tests are also common for studying mechanical properties [24].

If the material is brittle, such as gray cast iron, then the highest stress occurs at the point of fracture. If the material is ductile, such as aluminum, the stress peaks and then decreases prior to fracture. The peak, or maximum stress, is the point at which necking begins. Necking is the phenomenon where the maximum load at a point decreases due to the rapid decrease of cross sectional area at that point [24] . Figure 7 shows examples of stress-strain curves for brittle and ductile types of materials.

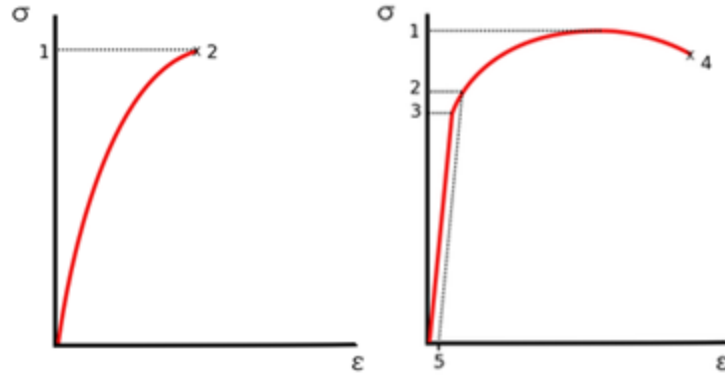


Figure 7. Sample stress-strain curves for brittle materials (left) and ductile materials (right). Note that on the brittle curve, the ultimate tensile strength (2) is the point of fracture. On the ductile curve, the highest stress is at (1) and the fracture stress is at (4), which is less than ultimate tensile strength [25].

The ultimate tensile strength, or simply tensile strength, of a material is the highest engineering stress reached prior to fracture. To determine the tensile strength, a universal testing machine is used to apply a load, or force, to a sample until failure. The system measures the load throughout the experiment. By measuring the sample dimensions prior to testing, tensile strength can be determined by the relationship.

$$\sigma_u = \frac{L_{max}}{A_i} \quad (7)$$

where σ_u is the tensile strength, L_{max} is the maximum load, and A_i is the initial cross sectional area of the sample. The fracture strength of the material is obtained from the load at fracture, L_f , even if this is not the highest load reached, such as for a ductile material. The fracture strength can be determined by the relationship.

$$\sigma_f = \frac{L_f}{A_i} \quad (8)$$

where σ_f is the fracture strength, L_f is the load at fracture, and A_i is the initial cross sectional area of the sample. For brittle materials, $\sigma_u = \sigma_f$, but for ductile materials, σ_u may exceed σ_f .

Ductility is the ability of a material to accommodate inelastic deformation without breaking. In the case of tension loading, this means the ability to stretch by plastic strain, but with creep strain sometimes contributing. Engineering strain is expressed as the ratio of total deformation to the initial dimension of the material body in which the forces are being applied [26]. The strain can be determined by the universal testing machine to measure the change in length of the sample during testing. If needed, an extensometer can be added to the setup to measure the change in sample length during load application. The engineering fracture strain is determined by the relationship,

$$\epsilon_f = \frac{L_f - L_i}{L_i} \quad (9)$$

where ϵ_f is the strain at fracture, L_f is the load at fracture, and L_i is the initial length of the sample [24]. On the stress-strain curve, ϵ_f is located at the same point as σ_f .

Initial portions of stress-strain curves from tension tests exhibit a variety of different behaviors for different materials. There may be a well-defined initial straight line, such as for many metals, where the deformation is mostly elastic. The elastic modulus, also known as Young's Modulus, or E , is the measure of stiffness of an elastic material that is used to characterize materials. Young's Modulus is obtained by using two points on the linear region of the stress-strain curve and the relationship,

$$E = \frac{\sigma_2 - \sigma_1}{\varepsilon_2 - \varepsilon_1} \quad (10)$$

where the subscripts 2 and 1 represent two different locations on the linear portion of the stress-strain curve as shown in Figure 8.

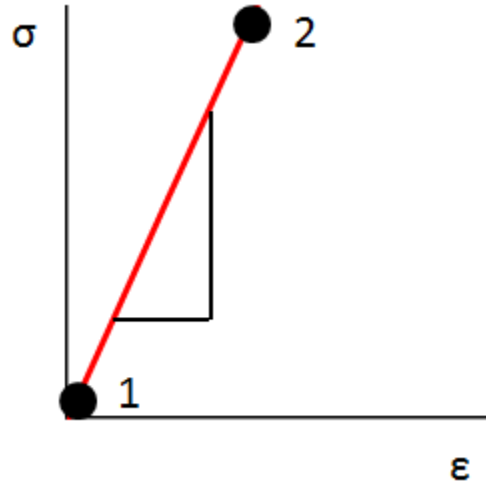


Figure 8. This plot shows the linear region of the stress-strain curve. This region is where Young's Modulus, or E, is determined by calculating the slope using two points on the linear portion of the curve.

3.3 Raman Spectroscopy

The phenomenon of inelastic scattering of light was first postulated by Adolf Smekal in 1923 and first observed experimentally in 1928 by Chandrasekhara Venkata Raman and K.S. Krishnan. Raman won the Nobel Prize in physics in 1930 for his experiment, and since then the phenomenon has been referred to as Raman spectroscopy [27].

Raman spectroscopy is a spectroscopic technique used to observe vibrational, rotational, and other low frequency modes in a system. It relies on inelastic scattering, also called Raman scattering, of monochromatic light, usually from a laser in the visible,

or near ultraviolet range. The laser light interacts with the molecular vibrations, phonons or other excitations in the system, resulting in the energy of the laser photons being shifted up or down [28]. This shift in energy gives information about the vibrational modes in the system. If the vibrational state of the molecule is more energetic than the initial state, then the emitted photon will be shifted to a lower frequency in order for the total energy of the system to remain conserved. This type of shift is called a Stokes shift. If the final vibrational state is less energetic than the initial state, then the emitted photon will be shifted to a higher frequency. This type of shift is known as an Anti-Stokes shift [28]. The typical Raman spectrum is normally measured in wavenumber, or inverse centimeters (cm^{-1}), and intensity in arbitrary units.

3.4 Raman Spectroscopy in Carbon Nanotubes

In the Raman spectra of graphite and single-walled carbon nanotubes (SWNTs), there are many features that can be identified with specific phonon modes and with specific Raman scattering processes that contribute to each feature [15]. Since mechanical, elastic, and thermal properties are strongly influenced by phonons, Raman spectra provide much information about the structure and properties of SWNTs.

While there are many phonon modes in SWNTs, only 10-15 are Raman active in the various chiral types of nanotubes. Popular modes for research in SWNTs are the radial breathing mode (RBM), D-, G-, and G' -bands, all shown in Figure 9. The RBM and G-band are first order Raman scattering events, while the D- and G' -bands are second order scattering events.

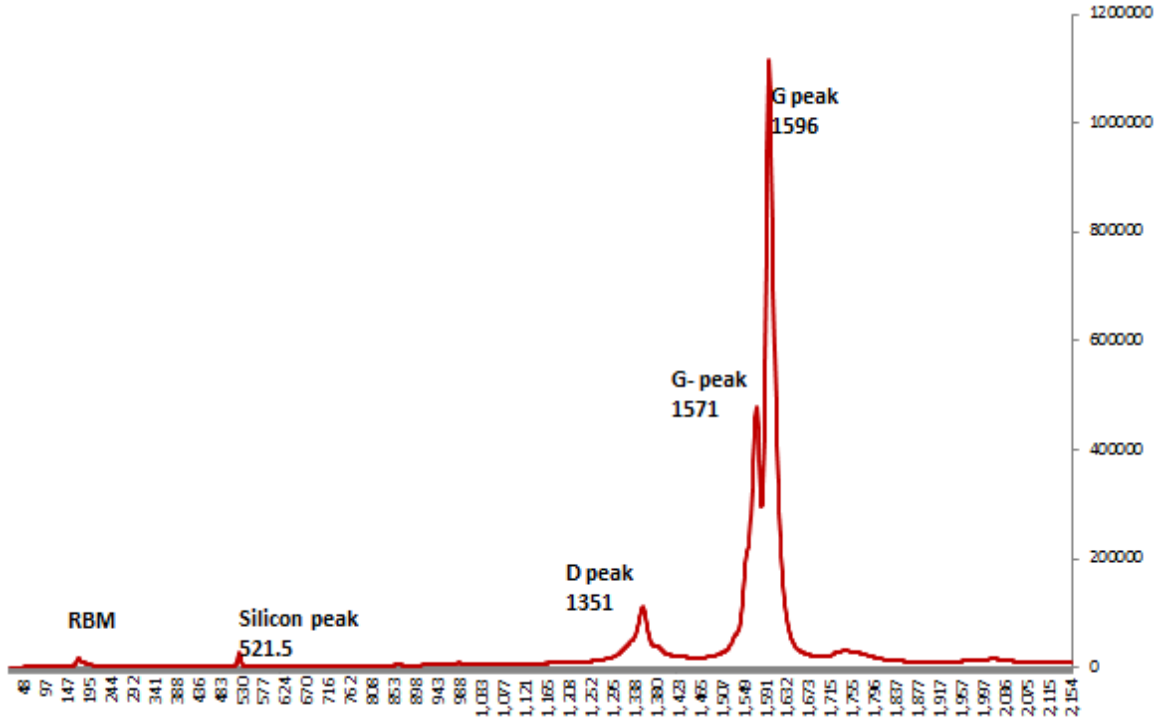


Figure 9. Example of a Raman spectrum for a SWNT thin film sample [29]. The radial breathing mode (RBM) peak is shown at the far left. The D and G peaks are shown at 1351 and 1596 cm⁻¹, respectively.

The RBM Raman features correspond to the coherent vibration of the carbon atoms in the radial direction, as if the tube were “breathing” [15]. This is a feature unique to CNTs and can be used to determine their presence. Additionally, the RBM can be used to determine the diameter of SWNTs through the relationship

$$d_t(nm) = \frac{248(cm^{-1}) * nm}{RBM_{peak}(cm^{-1})} \quad (11)$$

where d_t is the average nanotube diameter.

The G-band is located at 1596 cm⁻¹ in SWNTs and corresponds to the high energy phonon mode relative to the long axis of the carbon nanotube. In SWNTs, the G-band is composed of several peaks due to the phonon wave confinement along the SWNT

circumferential direction and symmetry-breaking effects associated with SWNTs. The G-band frequency can be used for (1) diameter characterization, (2) to distinguish between metallic and semiconducting SWNTs, through strong differences in their Raman lineshapes, (3) to probe the charge transfer arising from doping a SWNT, and (4) to study the selection rules in the various Raman scattering processes and scattering geometries [15].

The Raman D-band, or disorder band, is commonly used to estimate the amount of the defects in graphitic materials [30]. This peak is formed by phonon scattering due to defects in the lattice structure of the nanotube. The scattering is caused by dislocations in the lattice, Frenkel pairs, and impurities in the fabrication process. There is a direct relationship between peak intensity and the number of defects; a larger number of defects results in a higher peak intensity. Theoretically, for a perfect crystal there would be no noticeable D-band [30]. Additionally, sample purity can be investigated using the D/G band intensity ratio in the Raman spectra from SWNTs [15].

The G'-band is the dominant feature in the second order Raman spectra for SWNTs. Due to the larger dispersion of the G'-band, and because it is less sensitive to nanotube defects, many of the fundamental studies on the electronic and phonon properties of SWNTs have been done on the G'-band feature [15].

Most of the characteristic differences that distinguish the Raman spectra of SWNTs from the spectra of graphite are not evident in MWNTs [15]. This is caused by the large diameter of the outer tubes for typical MWNTs and the wide range of nanotube diameters. For example, the RBM signal from larger diameters is often too weak to

observe, and the additional inner tubes broaden the band when observable. This wider peak makes it more difficult to accurately determine tube diameter.

The Raman interest related to this research is the study of the damage to MWNTs caused by neutron irradiation. By applying the theory of SWNTs to MWNTs, we can use the D-band to study the peak intensity before and after irradiation. An increase in the peak intensity can be attributed to radiation damage. Using both the D- and G-band, the D/G ratio can be used to determine the sample structural purity before and after radiation. Any observable changes would be attributed to the effects of the neutron irradiation.

3.5 Neutron Interactions

Neutrons primarily interact with atomic nuclei. The two types of interactions are scattering and absorption, where scattering is the greatest importance in this work. When a neutron is scattered by a nucleus, its speed and direction change but the nucleus is left with the same number of protons and neutrons it had before the interaction. The nucleus will have some recoil velocity and it may be left in an excited state that will lead to the eventual release of radiation. When a neutron is absorbed by a nucleus, a wide range of radiations can be emitted or fission can be induced [31].

Scattering events can be subdivided into elastic and inelastic scattering. In elastic scattering, the total kinetic energy of the neutron and nucleus is unchanged by the interaction. A fraction of the neutron's kinetic energy is transferred to the nucleus. For a neutron of kinetic energy E encountering a nucleus of atomic weight A , the average energy loss is

$$E_{loss} = \frac{2EA}{(A + 1)^2} . \quad (12)$$

This expression shows that in order to reduce the speed of neutrons with the fewest number of elastic collisions, target nuclei with small A should be used. In general, after n elastic collisions, the neutron's energy is expected to change from the initial energy, E_0 , to the energy after n collisions, E_n by the relationship

$$E_n = E_0 \left[\frac{(A^2 + 1)}{(A + 1)^2} \right]^n . \quad (13)$$

For example, a 2 MeV neutron in carbon will require 119 collisions to reduce the energy to 0.025 eV, or to thermalize the neutron [31].

Inelastic scattering is similar to elastic scattering except that the nucleus undergoes an internal rearrangement into an excited state from which it eventually de-excites releasing radiation. The total kinetic energy of the outgoing neutron and nucleus is less than the kinetic energy of the incoming neutron; part of the original kinetic energy is used to place the nucleus into the excited state [31]. The net effect on the neutron is to reduce its speed and change its direction. If the energy of the nuclear excited states of the target nuclei are higher than the energy transferable by the neutron in the collision, then inelastic scattering is impossible. For example, the hydrogen nucleus does not have excited states, so only elastic scattering is possible.

3.6 Neutron Interactions in CNTs

Non-ionizing energy losses (NIEL) in CNTs result in knock-on damage, or atomic displacements from the lattice structure. In this mechanism, atoms are displaced from their stable location within the CNT if the energy transferred from the incident particle is greater than the displacement energy (E_d) binding the atom to its lattice location. The vacancy left by the displaced atom and the interstitial, or the newly displaced atom is called a Frenkel pair [32], as shown in Figure 10. NIEL radiation can generate numerous Frenkel pairs depending on both the incident particle energy and the binding energy of the lattice.

In addition to creating Frenkel pairs, the displaced atom can also form a cross-link as shown in Figure 11. Cross-linking can occur internally, between concentric tubes of the MWNTs, or externally between two different MWNTs. The cross-link occurs when the atom forms an ionic bond between the tubes rather than filling a vacancy or creating a Frenkel pair on a single nanotube.

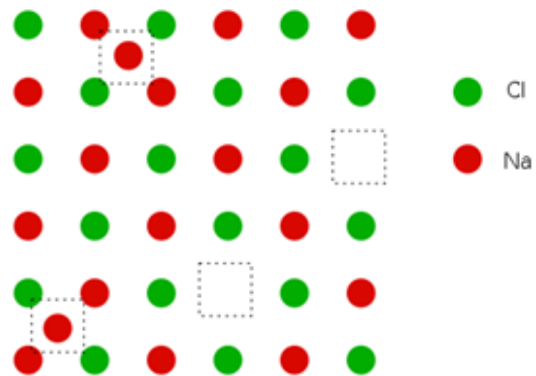


Figure 10. An example of two Frenkel defects within the NaCl structure. The empty boxes represent locations where the Na atoms were dislocated and the red circles with boxes around them represent the interstitial locations where they reattached to the structure [33].



Figure 11. The image on the left shows cross-linking externally between different SWNTs. The image on the right shows cross-linking internally between concentric tubes in an MWNT. In MWNTs, cross-linking occurs internally and externally from MWNT to MWNT. Reproduced with permission from Krashenikov, *et al.* [34].

IV. Methodology

Chapter Overview

This chapter provides a detailed explanation of the experimental methods used in conducting this research. The methodology is divided by respective experiment. Additionally, the procedure for sample irradiation is detailed.

4.1 Sample Preparation

Five panels measuring one square foot were received for the research. The panels were all from the same roll of MWNT ply. For this research, one panel was selected and cut to the required sample sizes for testing. The samples were then cleaned with isopropyl alcohol and rinsed with de-ionized water. Once the samples were dry, they were placed in vacuum and pumped down to a pressure of 5.1×10^{-5} torr for a period of 48 hours.

4.2 Sample Irradiation

Neutron irradiation was conducted at the Ohio State University Research Reactor (OSURR). The OSURR is an enriched U^{235} reactor with a maximum power of 500 kilowatts. For research purposes, the power is limited to 90%, or 450 kilowatts. The reactor is located inside of a 20 feet deep pool of water. The water provides cooling as well as neutron moderation and gamma shielding. The reactor has several different facilities that can be used for experimentation. For this research, the 20 foot dry tube was selected. This fixture was used in previous research and the flux is well characterized.

Additionally, using the dry tube allowed for all samples to be irradiated simultaneously, and ensured that all of the samples received the same dose.

The samples were mounted on a 4" × 4" sample holder made of Plexiglas. Holes were drilled in the plexiglas to allow for aluminum wire to be laced through and hold the samples to the sample holder as shown in Figure 12. Wire was chosen because tape was expected to fail during irradiation.

The dry tube is made of 6061 T6 aluminum and is 20.5' in length with a 7" outer diameter and 0.125" tube wall thickness. The tube is weighted with approximately 350 pounds of steel to provide negative buoyancy. There is an additional safety cap that provides shielding and moderation during experimentation that is put into place on top of the tube during irradiation. The dry tube location is shown in Figure 13.



Figure 12. This figure shows the samples on the plexiglas holder with the samples wired to the holder using 0.3" diameter aluminum wire.

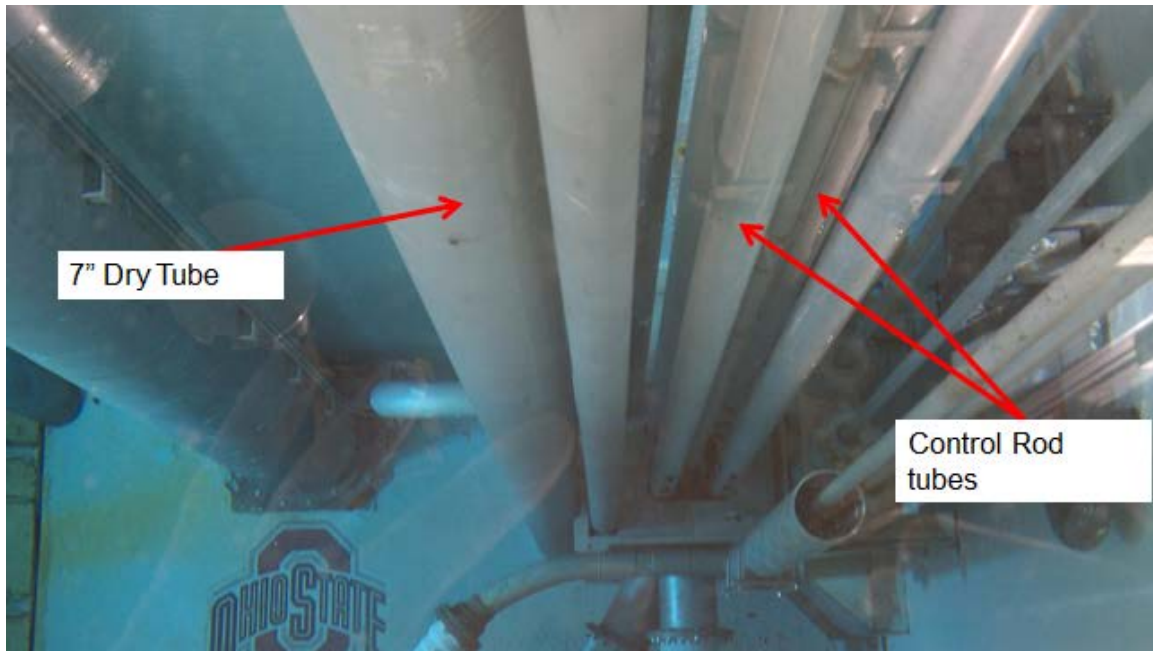


Figure 13. The OSURR as viewed from above looking into the cooling pool at the reactor. The dry tube is marked on the left and the reactor control rod tubes are also marked. The reactor is at the bottom of the pool.

The sample holder was then placed in a cadmium box mounted on the experimental apparatus that was lowered into the dry tube chamber. The cadmium box, shown in Figure 14, was constructed using 2 mm thick cadmium sheets. The purpose of the box was to harden the spectrum to better approximate a 1 MeV (Si-eq) neutron flux. Previous researchers conducted activation analysis to determine the flux profile in the dry tube fixture. The experimentally determined flux profile shows that the maximum flux of 2.78×10^{10} neutrons/cm²-s 1 MeV (Si-eq) is achieved at a location 13 inches from the bottom of the chamber [35]. The rope on the experimental apparatus was measured to ensure the proper placement of the samples and the apparatus was then lowered in to the chamber. A flashlight was used to confirm the orientation of the apparatus while it was being lowered into the chamber to make certain the MWNT side of the sample was

facing the reactor. The target fluence for this research is 10^{14} n/cm². The samples were irradiated for 90 minutes for a total fluence of 1.5×10^{14} n/cm².



Figure 14. This figure shows the sample holder with the mounted samples being placed into the cadmium box mounted on the apparatus. The rope shown on the left side of the apparatus is used to lower the entire setup into the dry tube chamber.

4.3 Mechanical Measurements

Tensile strength (TS) and Young's Modulus (E) were determined experimentally by conducting monotonic tension tests of the nanocomposite material. The tests were performed using the Material Test System (MTS) 810 servo-hydraulic test machine with a maximum load capacity of 22 kips (98 kN). The tests were all conducted at room temperature in the Mechanics of Aerospace Materials Laboratory at the Air Force Institute of Technology.

Sample size for the mechanical test was 8×90 mm. Samples were prepared for testing by attaching red composite tabs to the samples. The tabs, shown in Figure 15, are simply used to provide more material for the grips to lock onto so a sample will not slip from it under stress, and to help prevent samples being crushed by the jaws. The tabs were made 8 mm wide, the nominal width of each sample, and were cut 1" long to allow maximum surface area for the grip to lock onto. The tabs were attached to the samples using M-Bond 200 adhesive. The M-bond is an adhesive that is certified for strain gauge use and is used in routine stress analysis applications. A drop of M-bond was placed on each sample and spread out under the tab. The tab was held in place for 1 minute using thumb pressure and then allowed to cure for 30 minutes during the MTS warm-up cycle. Tabs were placed on both ends of the sample, on both sides, for a total of 4 tabs per sample. The final step of preparation was to measure each sample's width, thickness, and length so that the stress and strain could be accurately calculated. The length of the sample is the measured length exposed between the red tabs, or the length of the sample minus what will be inside of the grips of the MTS.



Figure 15. The upper sample shows the red tabs that have been attached to the sample for testing, as compared to the lower sample that has yet to be prepared.

Prior to testing, the MTS 810 was operated through a warm-up procedure for 30 minutes, in accordance with manufacturer's guidance. The procedure delivered a cyclic displacement command to the function generator which utilized a sine wave input with a frequency of 1 hertz (Hz) and amplitude of 10 mm. Following warm up, the test designed in the MultiPurpose TestWare (MPT) software for the experiment was selected. The test was designed for a 5 second ramp up to 100 N and then a steady increase in force until fracture, followed by a 5 second ramp down. The slow ramp up allows for the force to be added slowly and not as a quick shock to the sample. Data collection begins with ramp up and ends with ramp down, with data being collected every 0.5 seconds. The selected fields for data collection were force and displacement. The force recorded is the known value of the force applied to the sample by the MTS. The displacement recorded is a measure of the displacement of the gripper jaws during the test. The change in displacement of the jaws was used to measure the strain on the sample.

Using the displacement mode and manual control, the lower grip was moved to approximately 80 mm from the upper grip to allow for the sample to be mounted. The sample was mounted in the upper grip first, using an initial grip pressure of 500 psi. The lower grip was then carefully moved into position to lock the sample into place. After both grips were locked down at 500 psi, the sample orientation was checked to ensure it was level, allowing the force to be applied correctly along the desired axis. This was performed using a combination square placed on the lip of the lower grip to visually inspect that the sample was vertically level. After final adjustments, the grip pressure was increased to 1000 psi and the sample was ready for testing, as shown in Figure 16. The MPT software was then switched from manual to automated control and the experimental test was conducted. The test was performed until material failure, which occurred approximately after 1 minute. The MPT was put in manual mode and the sample was removed and a new sample was installed, repeating the procedure until complete.

The data set for each sample was saved for analysis. The MTS applied a known force to the sample in measured increments. By measuring the displacement of the sample, the stress versus strain curves for each sample could be generated using Equation (8) and Equation (9). Young's Modulus was calculated using Equation (10).



Figure 16. The sample mounted in the MTS 810 ready to begin the monotonic tension test.

4.4 EMI-SE Measurements

To measure the EMI shielding effectiveness of the nanocomposite, five 10×23 mm samples were selected from the twelve that were cut by the fabrication shop. These samples were selected based on how well they fit into the wave guide of the Agilent Technologies E8362B PNA Series Microwave Network Analyzer, as shown in Figure 17. The selected samples were numbered 7 through 11.



Figure 17. The fixture on the left is the waveguide used for sample mounting for network analyzer measurements. On the right is the shielding block used in calibration, and on the bottom left is a sample.

Prior to taking measurements, the network analyzer was calibrated to measure frequencies between 8.2-12.4 GHz (X-band) using the procedures provided by the manufacturer. Following calibration, the first sample was then placed in the cutout of the 1/4" inch X-band line measurement waveguide. The waveguide was then placed in the line adaptors between port 1 and port 2 of the network analyzer, as shown in Figure 18. The wave guide was secured using the 5/16" hex cap screws and the Agilent Technologies 0.9 N-m torque wrench. With the sample securely mounted, the analyzer was then used to measure the microwave signal along all four paths capable of being measured: reflection 1-1, reflection 2-2, transmission 1-2, and transmission 2-1. The reflection data was not saved but used as a visual check of the measurement prior to measuring transmissions (1-2, 2-1), which were saved and compared for this study. The measurements were made using the continuous sweep mode for 201 sweep points and with auto-correction on.



Figure 18. Photograph showing a sample being secured into the Agilent Technologies E8362B PNA Series Microwave Network Analyzer. The waveguide is secured by hex cap screws and nuts tightened to the torque specifications of the Agilent Technologies 0.9 N-m torque wrench. The left side is the port adaptor for port 1, and port 2 is on the right side of the photo.

After measuring and saving the data for each of the five samples numbered 7 through 11, the machine was re-calibrated as before and the next group of measurements was made. On each successive round of measurements, the next sample in numerical order was measured first, such that after 5 measurements, they were all measured at the same intervals following calibration. For example, for the second group, sample 8 was measured first after calibration and sample 7 was measured last prior to re-calibrating for the third group of measurements. The torque wrench was essential to insure that each sample was mounted in a consistent manner throughout the experiment. Additionally, the

samples were marked with an arrow so that they would always be placed in the wave guide in the same orientation, arrow facing up and the black, or MWNT, side always oriented facing port 1, as shown in Figure 19. After five rounds of measurements, with calibration in between and rotation of the measurement order, the pre-irradiation data was collected for analysis.

Following neutron irradiation, the EMI-SE measurements were conducted again, strictly adhering to the mounting procedure. There was a 96-hour delay in making the post-irradiation measurements to allow adequate time for radioactive decay of the neutron-activated material following the irradiation. The measurements were made a third and fourth time after irradiation, at 216 and 264 hours post-irradiation, respectively.



Figure 19. Photograph of the EMI-SE oriented face (MWNT ply) down. The five samples on the left are the samples that were neutron-irradiated. Sample 4 on the right was added to show the color change caused by irradiation. The numbers and arrow indicators are also visible.

4.5 Raman Spectroscopy

The Raman measurements began with the preparation of two samples. The first was a 10×10 mm piece cut from a larger strip after being vacuum stressed. In an

attempt to delineate damage to the MWNTs and the polymer, a second sample was made by adhering a strip of MWNT ply to a silicon wafer using double-sided tape. The critical step in sample preparation is to prevent the MWNT ply from wrinkling while attaching the MWNT ply. An uneven surface can interfere with the system's auto focusing capability and lead to high background noise in the measurement that can skew the data.

A test sample was first studied in the Renishaw inVia Raman Microscope to find out which one of the four lasers would provide the best results for this particular nanocomposite. After much trial and error, using many combinations of laser wavelength, power, and integration time, the 785 nm laser at 70 microwatts (μW) power was chosen. This laser provided the cleanest spectra with the least amount of background noise, while not damaging the sample. For the MWNT ply sample, a 5 second integration time was used while with the nanocomposite sample, a 30 second integration time was used.

Two spectral maps of the sample were collected in the same location, one pre- and the other post-irradiation. This allows for comparison of the same location under both conditions, and prevents non-uniformity in the sample from skewing the results. Circular maps were selected for this study and the system was programmed to make a circular map at 100 micron step sizes over a 3 mm diameter circle. Both samples were measured the same way for pre- and post-irradiation conditions, as shown in Figure 20 .

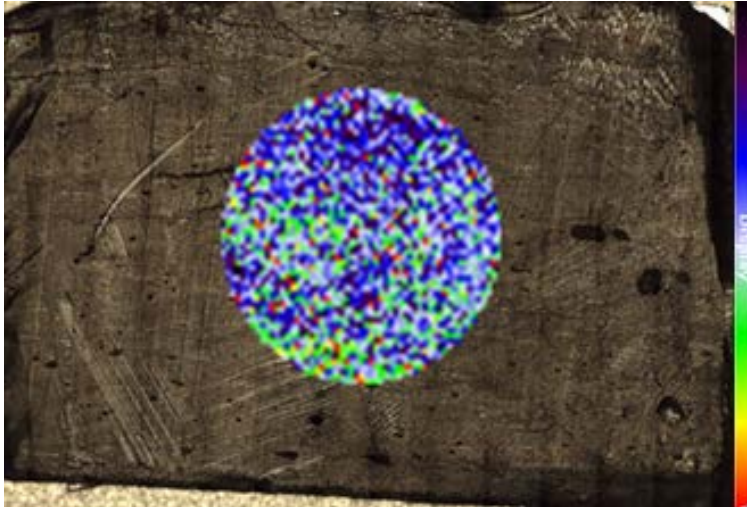


Figure 20. This image shows an example of the circular map made for the Raman study. The circle represents a 3 mm diameter with spectra recorded at 100 micron intervals for a total of 2496 data sets. In this example, the color represents the G peak intensity of the MWNT ply sample for the pre-irradiation measurement.

V. Results and Analysis

Chapter Overview

This chapter provides the experimental results of this research. The results are presented by experiment: mechanical (TS, E), EMI-SE, and Raman study.

5.1 Mechanical Measurements

The mechanical properties of tensile strength and Young's Modulus were experimentally determined pre- and post-irradiation. Samples 7 through 12 represent the pre-irradiation test samples and 13 through 18 are the post-irradiation samples. Samples 7 and 16 were testing anomalies, as described later, and excluded from this analysis.

The average stress-strain curve for the nanocomposite is shown in Figure 21. The pre-irradiation curve is the red dashed line and the post-irradiation curve is the blue solid line. The plot shows that the tensile strength of the irradiated sample is slightly higher than the pre-irradiated sample. The curve represents the average of 5 samples pre- and post-irradiation. The error bars represent the standard deviation of the data points averaged at that location. The shapes of the curves are indicative of a brittle material, as shown in the sample stress-strain curve of Figure 7. From the stress-strain curve, it can also be determined that Young's Modulus increased with irradiation. This is interpreted from the curve as the slope of the blue curve is slightly greater than the red curve. An increase in E means there is a reduction in elasticity.

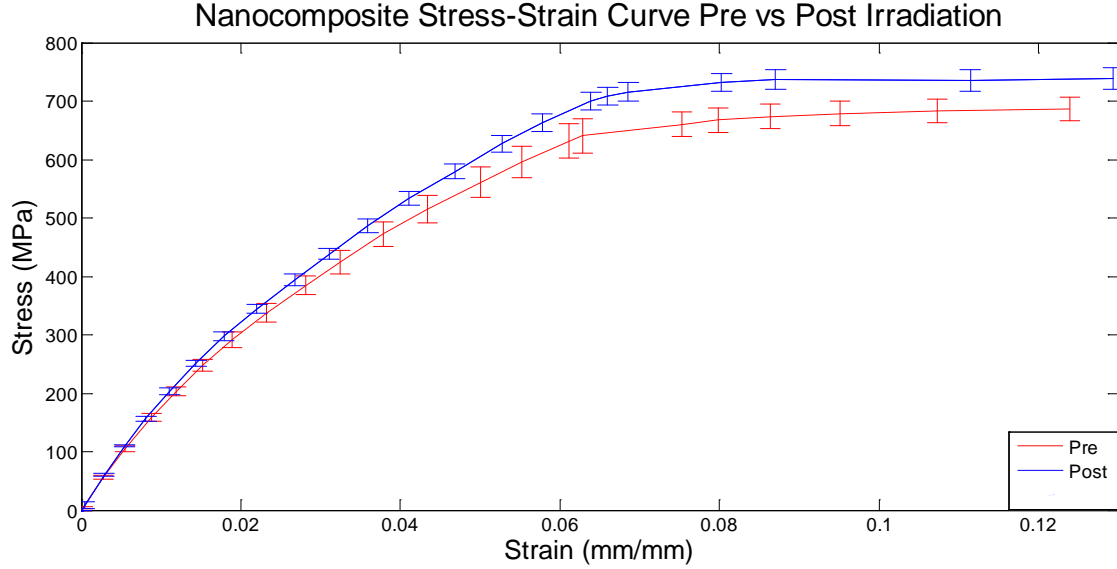


Figure 21. The average stress vs. strain curve for the pre- and post-irradiation samples. The pre-irradiation curve is in red and the post-irradiation curve is in blue.

The results of the monotonic tension testing are shown in Table 2. The average tensile strength of the pre-irradiated sample was 686 ± 18 MPa, while the post-irradiated sample was 727 ± 22 MPa. This is an average increase of 41 MPa in tensile strength following neutron irradiation, or a 6% increase over the pre-irradiated sample. Using the individual stress-strain curves, E was calculated for every sample. The average E for the pre-irradiated sample was 17 ± 0.9 GPa, and 19 ± 0.5 GPa after irradiation, as shown in Table 2. This is an average increase in E of 1.7 GPa following irradiation, or a 10% increase over the pre-irradiation value.

The increase in tensile strength and E is attributed to the effects of neutron irradiation. Figure 21 shows that the increase was not large. Taking into account the error shown on the plot by the error bars, the increase is insignificant in terms of design.

Table 2. The average tensile strength and Young's Modulus for the pre- and post-irradiation measurements.

Fluence 1.5×10^{14} n/cm ²	Tensile Strength (MPa)	Young's Modulus (GPa)
Pre-Irradiation	686 ± 26	17 ± 4
Post-Irradiation	727 ± 27	19 ± 4
% Increase	6%	10%

A material subjected to displacement damage, in this case by neutron irradiation, often reduces its mechanical strength. In this research, a slight increase was observed, which is counterintuitive. This is postulated to be the results of the effect of radiation on the polymer. Neutron irradiation leads to displacement damage in the polymer matrix. In polymers, the rupture of chemical bonds usually results in one of two sequels: cross-linking or scission [36]. Which sequel occurs depends on the polymer type. The resin used in the composite is bismaleimide, which is known as a brittle epoxy, made more so by irradiation [9]. Epoxy resins, such as bismaleimide, are known to have a cross-linking reaction when irradiated. Polymers which tend to cross-link show an increase in strength and toughness; however, they ultimately become brittle [36]. Other studies on the effects of neutron irradiation on epoxies have been conducted. It has been concluded that neutron irradiation induces cross-linking of polymeric chains and leads to a depolymerization which results in embrittlement of the epoxy, or polymer [37].

A slight increase in strength and embrittlement were both observed in this research as reported in Table 2 and illustrated in Figure 21. These results are attributed to the cross-linking of the polymer chains following radiation induced damage as described above, which resulted in an increased tensile strength. Additionally, the breaking of bonds shortens the polymer chains, reducing the polymer ductility, thereby increasing the brittleness of the polymer.

The tested samples are shown in Figure 22. The samples all exhibit similar fracture patterns, with sample 9 being unique, in that it failed in two locations simultaneously. Sample 16, as discussed previously, was an anomaly. It was not tested to failure because the tabs slipped off of the sample prior to the sample failing. Sample 7 was omitted as it was the first sample tested after adjustments were made to the test program in the MTS software. While the data was valid, it was omitted from the study due to the slight variation in MTS parameters. Optical images of the fractures are shown in Figure 23. The pictures show that the E-glass woven fiber bundles were loaded to failure. The MWNT plies stretched until the E-glass failed. At that point, the MWNTs failed immediately as the E-glass layers provide the strength and structure to this nanocomposite.

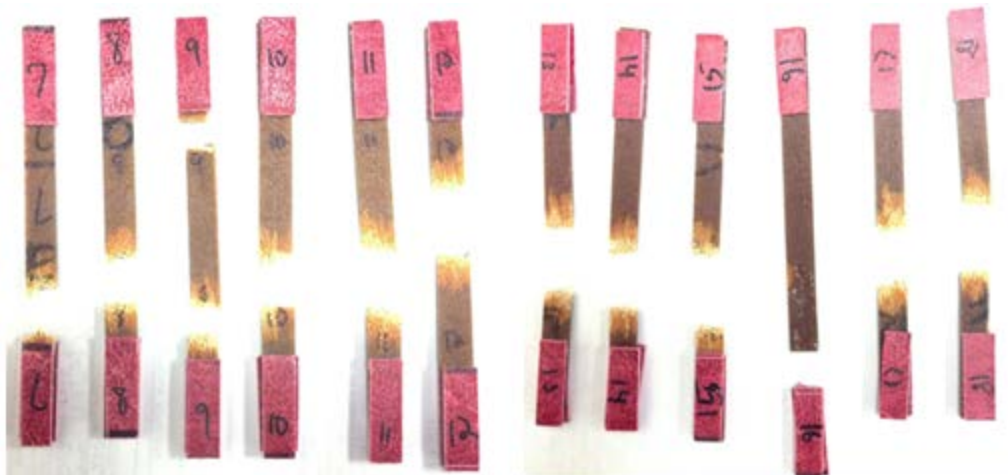


Figure 22. Photograph showing all of the samples tested to failure except for sample 16. The tabs on the bottom of sample 16 failed to remain adhered to the sample, and when the sample slipped out, it was not tested to failure. Sample 9 is unique to the sample set in that it failed in two locations simultaneously.

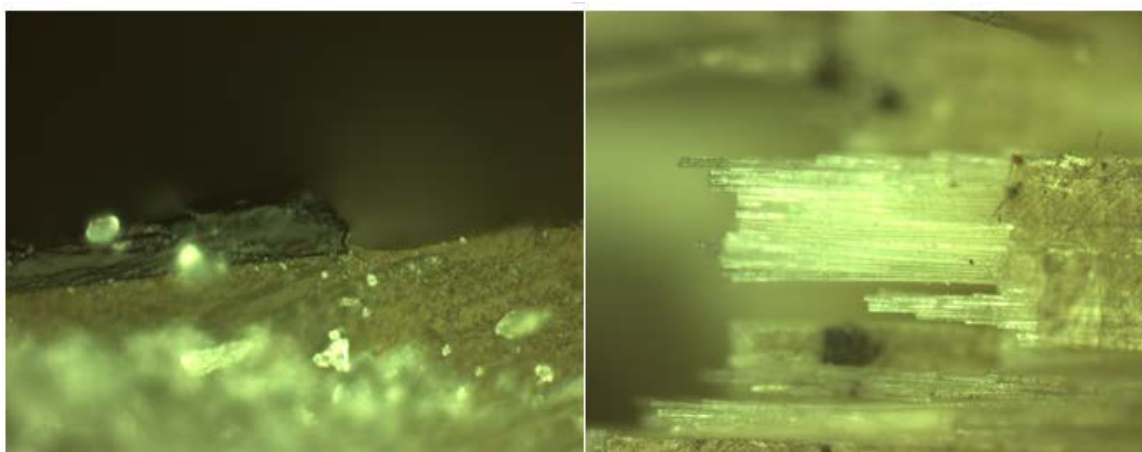


Figure 23. Images taken from an optical microscope. The image on the left is at (50× magnification) and shows the edge of the MWNT ply. The image on the right is at (10× magnification), and is a close up of one fiber bundle showing the fracture of the E-glass.

5.2 EMI-SE

The EMI-SE measurements were made at four different time intervals relative to the neutron irradiation, as discussed in the methodology section of this paper. All measurements for each sample were plotted on the same graph. The blue curve indicates

the pre-irradiation measurement. The green, red, and purple curves represent post-irradiation measurements at 96, 216, and 264 hours after irradiation, respectively. Each curve is an average of the 3 measurements made at each interval and then plotted using a Savitsky-Golay smoothing filter that is a built-in function of MATLAB.

Figure 24 shows that sample 7 had an initial increase in EMI-SE of approximately 9 dB, and maintained that increase until after 264 hours following irradiation, when the EMI-SE returned to within 1 dB of its original value. The 1 dB increase represents an increase of 26% in shielding effectiveness.

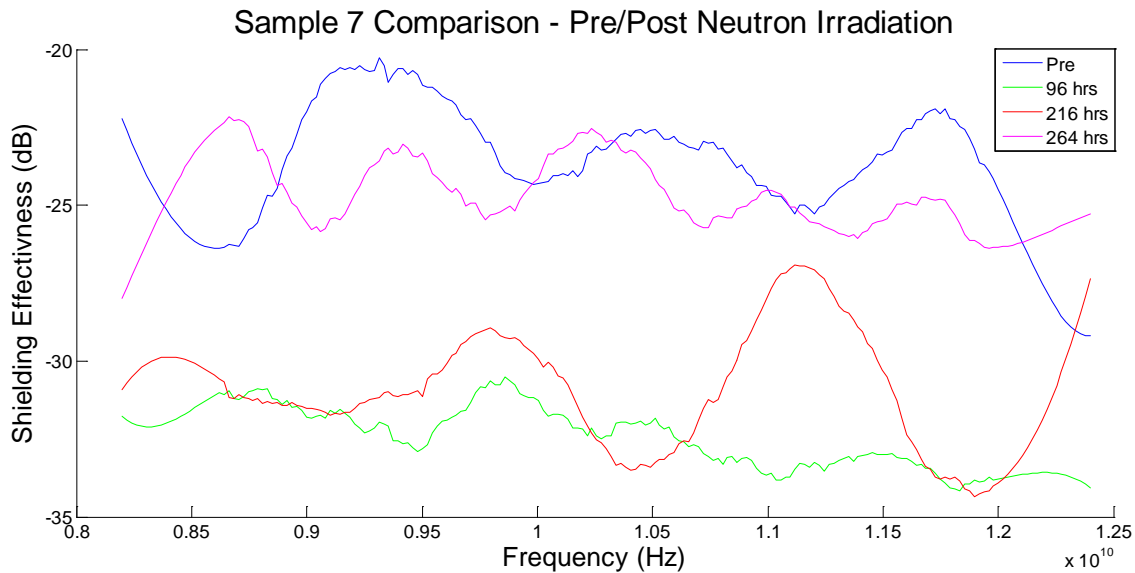


Figure 24. The EMI-SE measurements for sample 7 at four different time intervals relative to neutron irradiation. The time intervals are: Pre-Irradiation, 96 hours post-irradiation, 216 hours post-irradiation, and 264 hours post-irradiation.

Sample 8, shown in Figure 25, exhibited similar behavior to sample 7. The difference in samples 7 and 8 is that sample 8 returned to its pre-irradiation EMI-SE around 216 hours instead of between 216 and 264 hours. The initial increase in EMI-SE

is approximately 9 dB, which indicates nearly a factor of 10 increase in EMI-SE. The final value, while near the original, is an increase of 26% in SE.

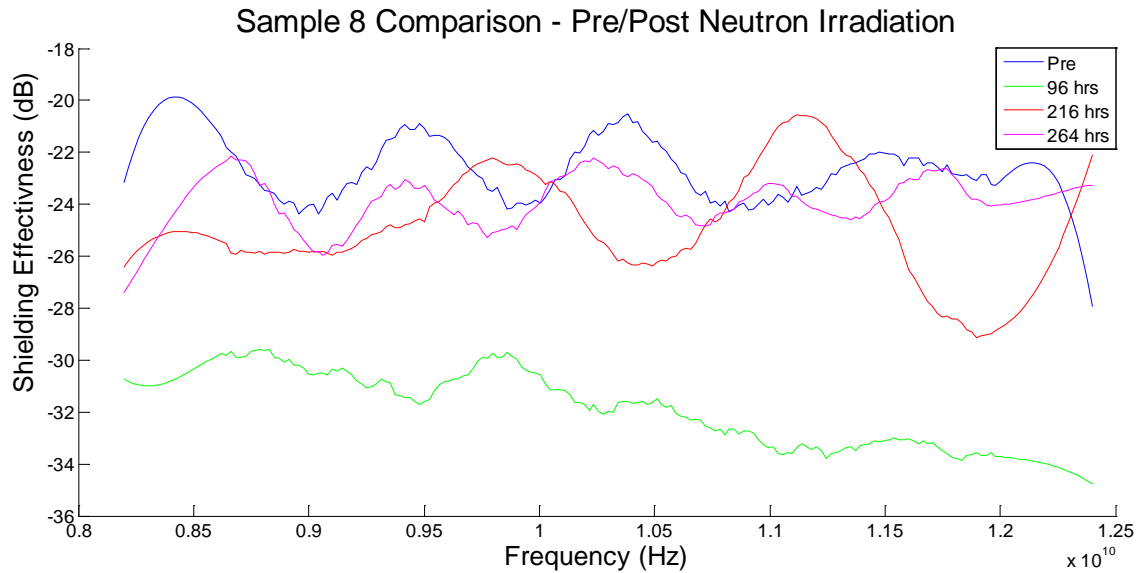


Figure 25. The EMI-SE measurements for sample 8 at four different time intervals relative to neutron irradiation. The time intervals are: Pre-irradiation, 96 hours post-irradiation, 216 hours post-irradiation, and 264 hours post-irradiation.

Sample 9 had varied results, as shown in Figure 26. This sample had essentially no change during any of the measurements in the cycle. The slight fluctuations in the plot can be explained as noise. Similar to samples 7 and 8, the sample 9 EMI-SE is at the original EMI-SE at 264 hours.

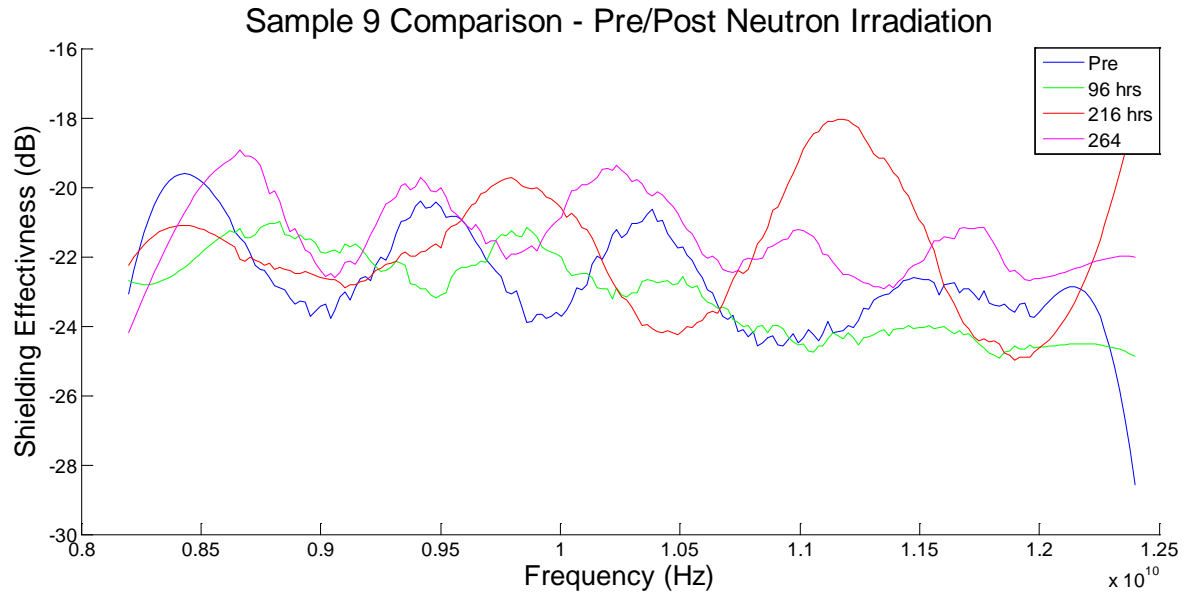


Figure 26. The EMI-SE measurements for sample 9 at four different time intervals relative to neutron irradiation. The time intervals are: Pre-irradiation, 96 hours post-irradiation, 216 hours post-irradiation, and 264 hours post-irradiation.

Sample 10 is similar to sample 7, with less of an increase in EMI-SE following irradiation. Figure 27 shows that the initial increase in EMI-SE is approximately 3 dB, which represents an approximate 100% increase in EMI-SE. At 264 hours, there is a 1 dB increase over the original value, resulting in an increase in EMI-SE by 26%.

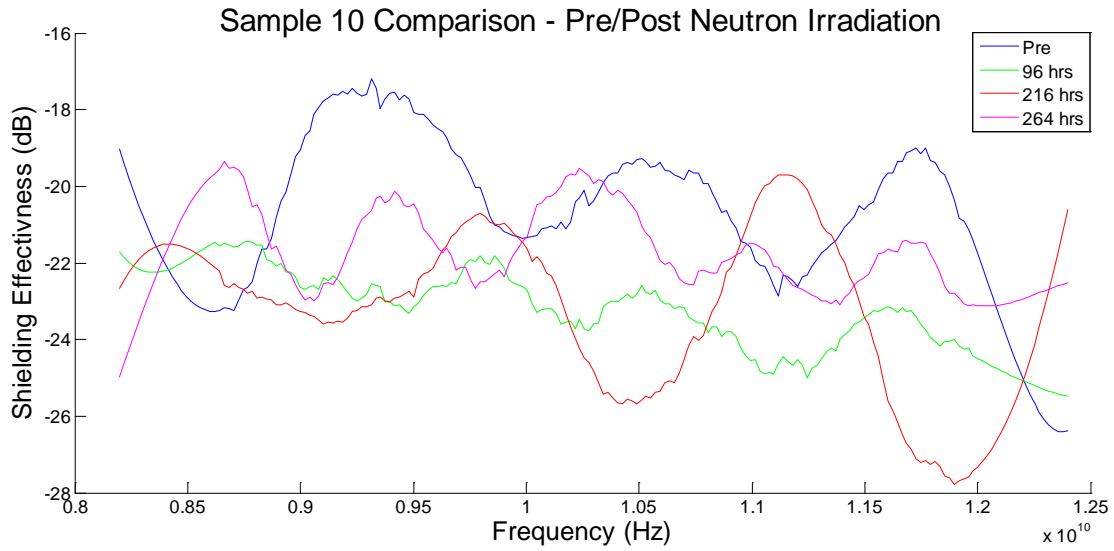


Figure 27. The EMI-SE measurements for sample 10 at four different time intervals relative to neutron irradiation. The time intervals are: Pre-Irradiation, 96 hours post-irradiation, 216 hours post-irradiation, and 264 hours post-irradiation.

Sample 11 is also similar to sample 7, with less of an increase in EMI-SE following irradiation. Figure 28 shows that the initial increase in EMI-SE is approximately 11 dB, which represents an approximate increase in EMI-SE by a factor of ten. At 264 hours, there is a 1 dB increase over the original value, resulting in an increase in EMI-SE by 26%.

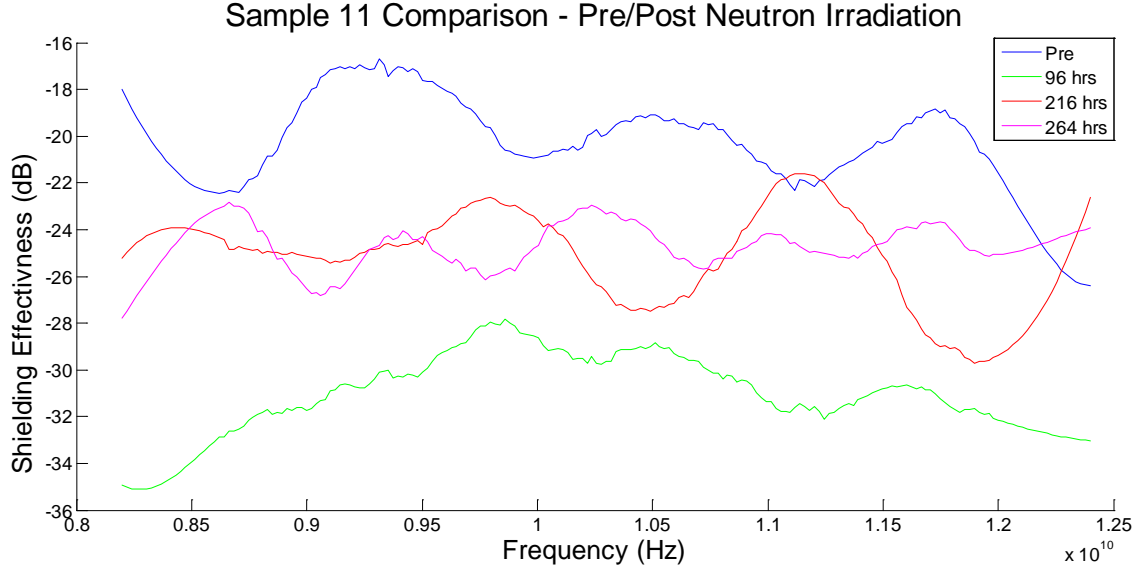


Figure 28. The EMI-SE measurements for sample 11 at four different time intervals relative to neutron irradiation. The time intervals are: Pre-Irradiation, 96 hours post-irradiation, 216 hours post-irradiation, and 264 hours post-irradiation.

The results of this experiment are consistent with [3], which found little change in the EMI-SE after both neutron and electron irradiation closely resembling the results in this research. Table 3 shows the average EMI-SE of all samples at the four measurement intervals. Figure 29 is a plot of the average value of all the samples at each point of the frequency range while Table 3 shows the average values across the frequency range. The column labeled \pm is the standard deviation of the mean EMI-SE determined from three measurements of the EMI-SE across the 201 microwave frequencies measured on each sample. An increase of 6 dB, or an approximately 400% increase in EMI-SE, was observed at 96 hours after irradiation. This change decreased over time and returned to within 1 dB, or a maximum 26% increase above the pre-irradiation value after 264 hours.

Table 3. Mean EMI-SE by sample at each tested interval.

	Pre		Post 96		Post 216		Post 264	
Sample	Mean EMI-SE (db)	± (dB)	Mean EMI-SE (db)	± (dB)	Mean EMI-SE (db)	± (dB)	Mean EMI-SE (db)	± (dB)
7	-23.73	0.06	-32.45	0.04	-30.89	0.04	-24.72	0.05
8	-22.68	0.07	-31.88	0.04	-24.87	0.05	-23.90	0.05
9	-22.70	0.07	-23.09	0.06	-21.77	0.05	-23.79	0.06
10	-20.76	0.07	-23.21	0.06	-23.23	0.05	-21.73	0.06
11	-20.33	0.07	-31.05	0.05	-25.17	0.05	-24.72	0.05
AVG	-22.04	AVG	-28.34	AVG	-25.19	AVG	-23.77	

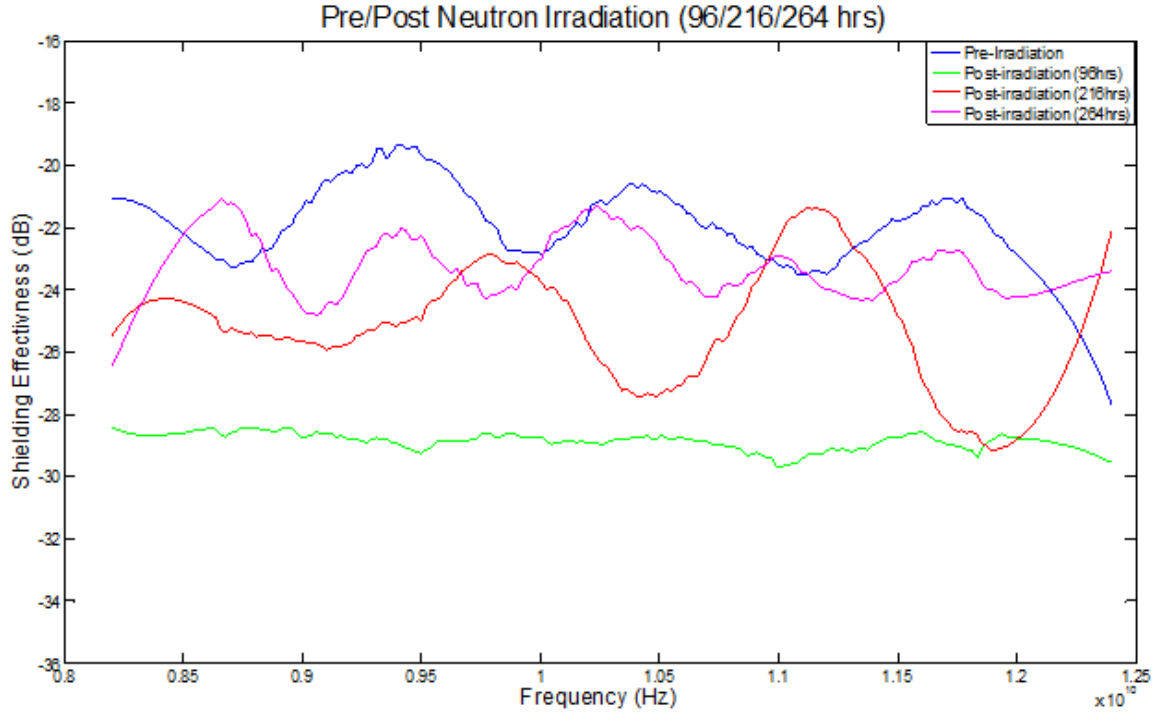


Figure 29. Average EMI-SE results plotted by time interval. In sequential order, the blue curve represents the pre-irradiation measurement, the green curve represents 96 hours post-irradiation, the red curve represents 216 hours post-irradiation, and the magenta curve represents 264 hours post-irradiation.

The ratio of shield thickness to skin depth is essential in the determination of SE. Since skin depth is calculated using conductivity, Equation (6), there is a direct relationship between conductivity and SE. As conductivity increases, skin depth decreases, resulting in higher EMI-SE. The increase in EMI-SE in this research is attributed to the increase in conductivity of the sample following neutron irradiation.

The MWNTs were added to the composite for the purpose of increasing the conductivity. Following irradiation, the conductivity increased. This increase is attributed to the displacement damage in the MWNT plies resulting from the irradiation. Neutrons striking the nanotubes with sufficient enough energy to displace atoms from the lattice do so, leaving vacancies. These atoms can displace other atoms causing cascade

displacements, but will eventually fill vacancies that were initial defects or created by knock-on displacement of another atom during irradiation [34]. Some atoms may fill in interstitial spaces. Figure 30(a) shows the displacement damage caused to a single walled nanotube, Figure 31(b) shows the annealing of the damage. For a measureable decrease in conductivity, there would need to be a significant amount of displacement damage to the nanotube.

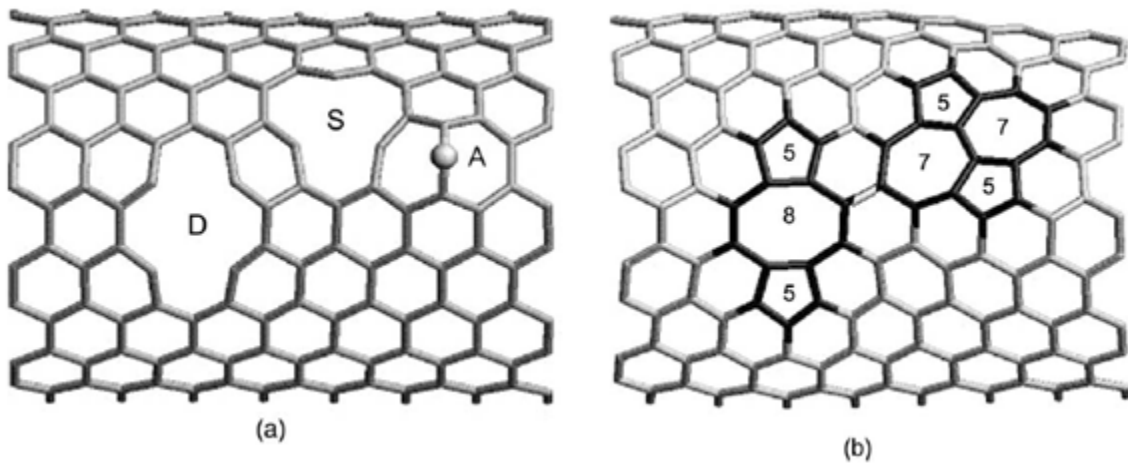


Figure 30. Front walls of one and the same SWNT just after impact (a) and annealing (b). During annealing, the double vacancy (D) and the single vacancy (S) are transformed into non-hexagonal rings. Reproduced with permission from Krashenikov, *et al.* [34].

The samples studied are MWNTs, and when the atoms are displaced, they can fill vacancies on the nanotube, but they can also fill those vacancies on the other concentric nanotubes, or neighboring MWNTs [36]. This effect, known as cross-linking, is shown in Figure 31. Cross-linking is responsible for the increases in conductivity by increasing the number of electron conduction paths through the tubes.

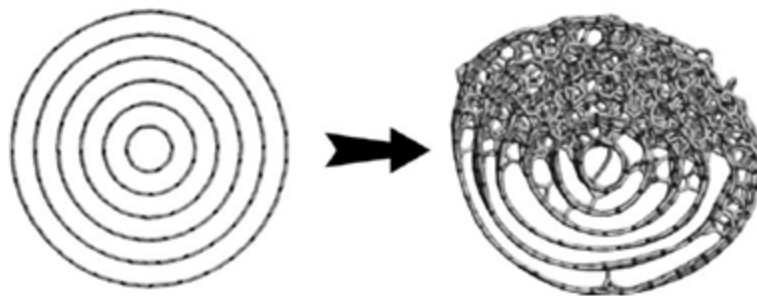


Figure 31. A side view of a MWNT before (left) and after (right) irradiation. The right hand image shows the cross-linking that can occur in the MWNT as atoms are displaced. Rather than fill vacancies along the tube it was displaced from, it can bond across tubes, cross-linking them together. Reproduced with permission from Krashenikov, *et al.* [34].

While this explains the increase in EMI-SE, it does not explain the return to near pre-radiation values over time. Displacement damage annealing in carbon nanotubes occurs at temperatures greater than 300 °C [34]. The samples studied in this research were not annealed at high temperature. The samples were stored at room temperature and at standard atmospheric pressure. As previously mentioned, neutron irradiation can cause cross linking of polymer chains [37], similar to cross-linking in the nanotubes. If the polymer adds to the overall conductivity of the composite, then cross-linking of polymer chains would increase conductivity. Sonkawade *et al.* also observed an increase in conductivity following neutron and gamma irradiation that was attributed to the cross-linking of polymer chains [38]. If the damage to the polymer anneals over time, this would explain the reduction of the EMI-SE over time.

5.3 Raman Spectroscopy

Following the collection of Raman spectra the MWNT ply and the nanocomposite sample were analyzed. The first analysis conducted was a comparison of pre- and post-

irradiation spectra for the same location. The Renishaw Wire software was utilized to first conduct a Voight curve fit of every data point. The backgrounds were then subtracted and the curves were normalized to the peak of the G-band for comparison, as shown in Figure 32. The plot shows the large increase in the peak of the D-band following irradiation of the MWNT ply sample. The D-band, or disorder band, is used to estimate the amount of defects of CNTs. An increase in the intensity of the D-band is indicative of increased damage to the CNTs.

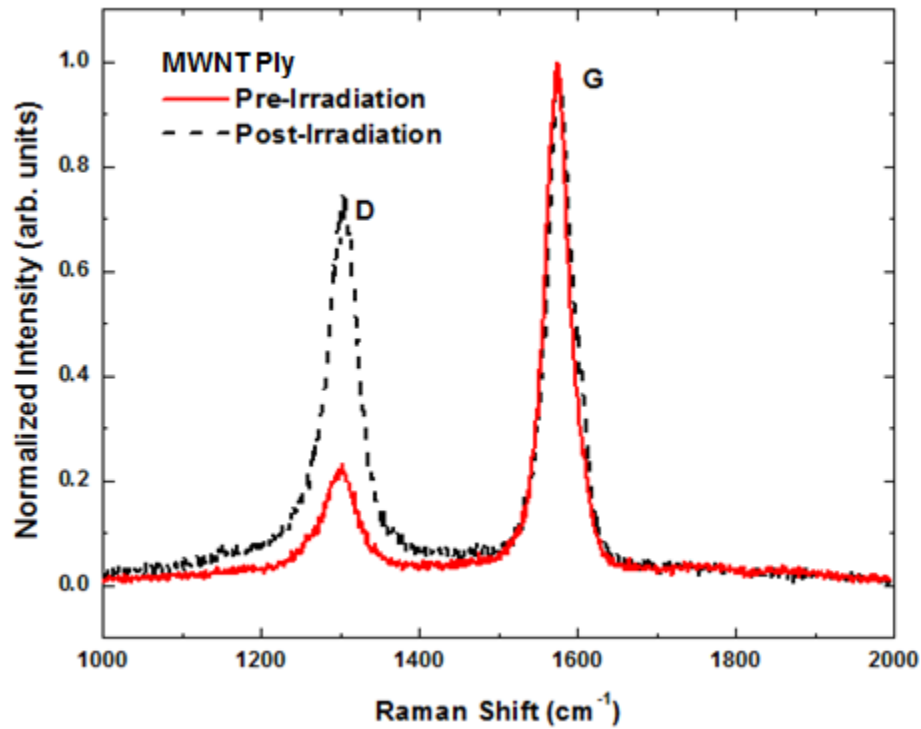


Figure 32: The Raman spectra of the MWNT ply sample with normalized intensity. The red curve represents the pre-irradiation spectrum and the black curve represents the post-irradiation spectrum. Of note is the large increase in the D-peak due to neutron induced damage of the MWNTs during irradiation.

Another method of studying CNT sample purity is to measure the ratio of the D-G band intensities. Normalized D/G ratios were plotted on 2D maps for comparison, as

shown in Figure 33 and Figure 34. The average D/G ratio of the pre-irradiation MWNT ply is 0.19 ± 0.04 (arb. units) across the surface, while the average D/G ratio of the post-irradiation MWNT ply is 0.48 ± 0.11 (arb. units). These results are consistent with literature describing similar measurements [15]: the damage to the CNTs from neutron irradiation causes the D-band intensity to increase, which causes an increase in the D/G ratio.

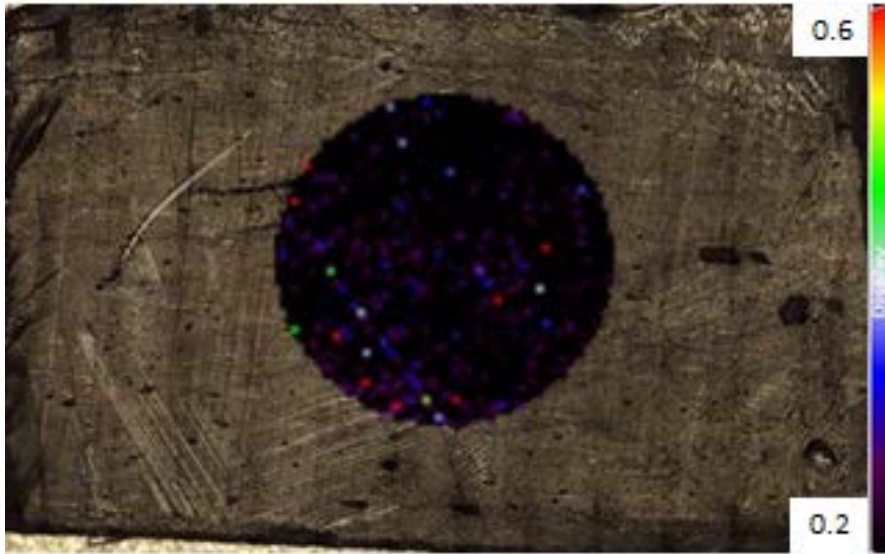


Figure 33. Normalized D/G ratio for the pre-irradiation MWNT ply sample. The color scale on the right represents intensity (arbitrary units) of the D/G ratio. The sample appears mostly black, which is a visual depiction of the calculated average D/G ratio of 0.19 ± 0.04 .

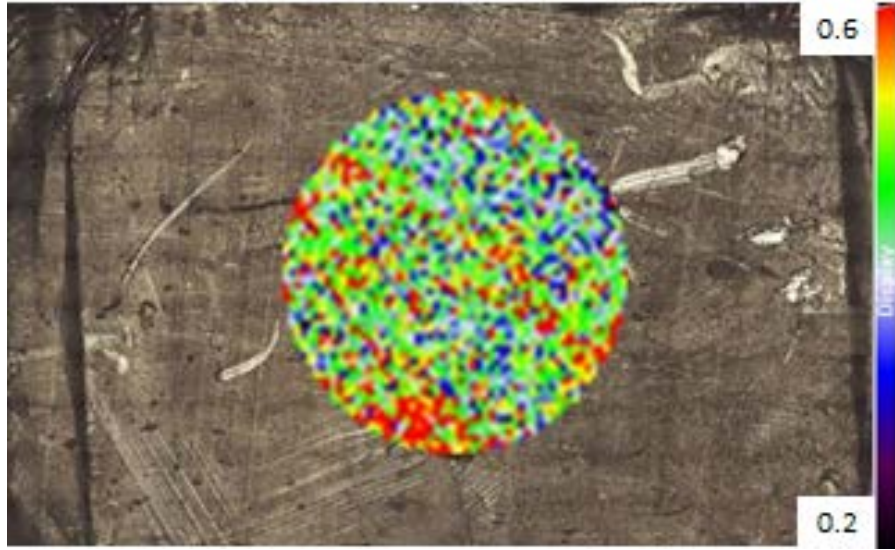


Figure 34. Normalized D/G ratio for the post-irradiation MWNT ply sample. The color scale on the right represents intensity (arbitrary units) of the D/G ratio. The sample appears mostly green, which is a visual depiction of the calculated average D/G ratio of 0.48 ± 0.11 .

In an effort to correlate the D/G ratio change to the observed displacement damage, a mathematical approach was taken to make a valid estimate. The displacement energy for a carbon atom is 20 eV [34]. Based on the mass difference between the carbon atom and a neutron, it requires a neutron with at least 240 eVs of energy to displace a carbon atom. Using Table 3.24 in [32] and making the assumption that carbon and silicon are similar, the NIEL loss can be approximated as $1 \text{ keV cm}^2/\text{g}$. Multiplying by the area density of the MWNT plies, 11 g/m^2 , the average NIEL loss is 1.1 eV per neutron. A model using Monte Carlo N-Particle (MCNP) Transport Code was used to simulate the number of neutron interactions in a carbon sample measuring $1 \text{ cm} \times 1 \text{ cm} \times 0.003 \text{ cm}$, where 0.003 cm is the nominal thickness of 2 plies of MWNTs. The results of the simulation show that approximately 1 out of every 200 neutrons interact with a MWNT ply. Since only one neutron interacts with the composite, the average energy of

200 neutrons is imparted by a single 220 eV neutron. Not all of the energy will be used to displace carbon atoms. Some energy will be consumed through various other mechanisms, such as scattering. Assuming 75% of the energy is used to displace carbon atoms, then each neutron will displace 2 atoms directly. The secondary displacements will be disregarded for now.

To estimate the number of carbon atoms per sample, the area density, 0.0011g/cm^2 , is divided by the atomic mass of the carbon atom, $2.32 \times 10^{-23}\text{ g/atom}$. Since the sample area is 1 cm^2 , this yields a value of $4.74 \times 10^{19}\text{ atoms/sample}$. The fluence used to irradiate was $1.5 \times 10^{14}\text{ neutrons/cm}^2$. Multiplying the number of neutrons by the average NIEL per neutron yields a total NIEL of $1.65 \times 10^{14}\text{ eV}$ for the sample. If all energy is used to displace carbon atoms, then a total of 6.9×10^{11} carbon atom displacements are possible. Assuming the sample begins with approximately 5% vacancies [39], the existing vacancies are 2×10^{18} vacancies per sample. To have a 150% increase in D/G ratio as shown in the Raman study, the number of vacancies must increase to 5×10^{18} per sample assuming that the D/G ratio change is linearly related to the number of defects. Since the number of defects created does not support an assumption of linearity in this relationship, there seems to be a nonlinear aspect to the correlation between the defect creation rate and the D/G ratio. Based on the results of this study, it is likely the relationship is not linearly dependent on displacements and that there are other factors involved that were not considered.

The nanocomposite sample did not provide the same quality of data that the MWNT ply sample provided. The data generated for the nanocomposite had an extremely inconsistent background signal that fluctuated to the point where it was

impossible to subtract. Additionally, the very low signal-to-noise ratio made it difficult to normalize the spectra. Figure 35 shows a comparison of the spectra for a single location pre- and post-irradiation. Additional single point spectra are shown in Appendix B.

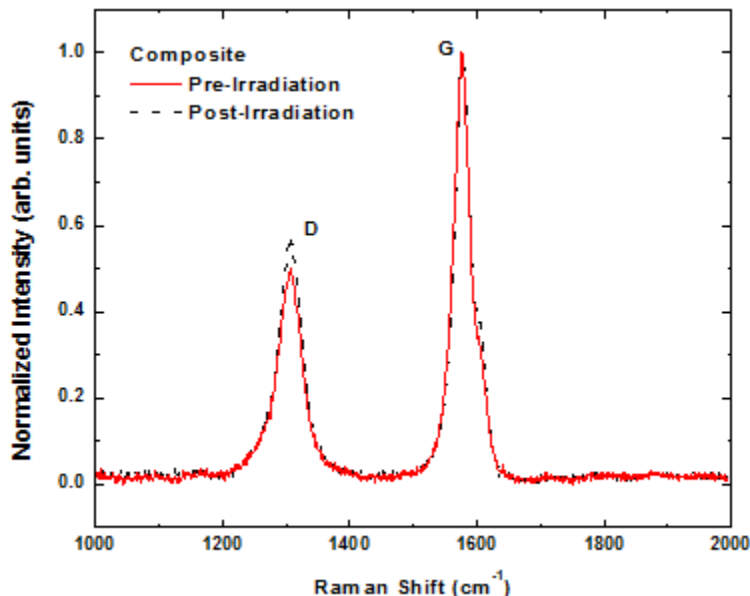


Figure 35. A single point Raman spectra of the nanocomposite sample with normalized intensity. The red curve represents the pre-irradiation spectrum and the black curve represents the post-irradiation spectrum. Of note is the small increase, approximately 0.05 (arb. units), in the D-peak due to neutron damage of the MWNTs during irradiation.

After failing to create a worthwhile 2D plot of the D/G ratios similar to the MWNT ply sample, a new analysis of the nanocomposite was conducted. The pre- and post-irradiation spectra were analyzed visually to locate data points where each spectrum showed small amounts of background noise and a high signal-to-noise ratio. When the pre- and post-irradiation spectra both met the criteria at the same location, it was deemed

valid and selected for analysis. This process was repeated until 5 data points were selected, giving a total of 10 data files (pre/post) to analyze.

The files were individually curve fit and backgrounds were subtracted for each file. The Renishaw Wire software was then used to determine the peak intensities of the D and G peaks. Using this data, the D/G ratios were calculated for the pre- and post-irradiation sample of the nanocomposite. The pre-irradiation average D/G ratio was calculated as 0.58 ± 0.1 (arbitrary units). The average D/G ratio after irradiation was found to be 0.62 ± 0.1 (arbitrary units). The averages are well within the error, so the analysis shows that there was little to no change following neutron irradiation.

While the composite sample did not yield confirmatory results indicating damage in the SWNT plies, it may have yielded something of value. While comparing the spectra at a single location, a new phenomenon was noticed while zooming in on the G peak. A shoulder at approximately 1605 cm^{-1} was observed on both pre- and post-irradiation spectra as shown in Figure 36. Comparing spectra for a single location, pre- and post-irradiation, show that the shoulder peak intensity increases slightly following irradiation. This shoulder is known as the D'-peak, which is known to appear at $1605\text{-}1615 \text{ cm}^{-1}$ for glassy carbon [40]. Glassy carbon has been shown to have a fullerene-related structure, which refers to any molecule made of carbon in the form of a sphere, ellipsoid, or tube. The MWNT does have a fullerene-related structure, so a D'-peak is normal; however, it was not as pronounced in the MWNT ply sample. The fact that it is more pronounced in the composite sample suggests that the polymer may affect this feature in Raman spectroscopy. If this feature can be attributed to the polymer, the

change in D' peak intensity may be a direct correlation to the damage to the polymer during irradiation.

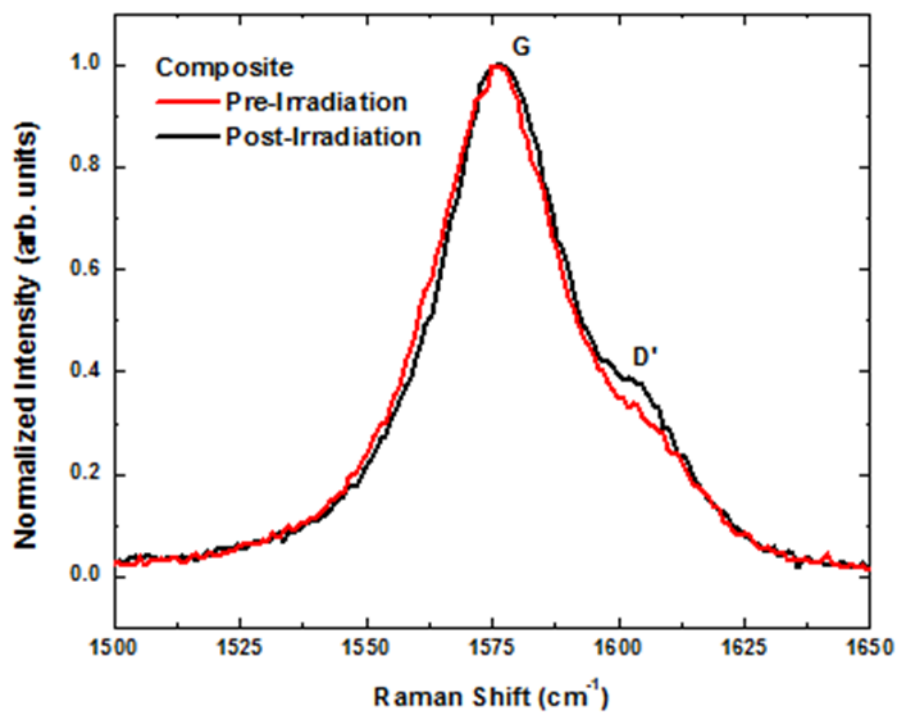


Figure 36. Single point Raman spectra of the pre- and post-irradiated nanocomposite sample. The focus of this spectra is to show the change in the D'-peak before and after irradiation.

VI. Conclusions and Recommendations

Chapter Overview

This chapter provides the summary of results and conclusions of the research. Additionally, recommendations are provided for future research in the area of radiation effects on nanocomposite materials.

6.1 Conclusions

The goals of this research were to study the changes to tensile strength and EMI-SE effectiveness of nanocomposite materials due to neutron irradiation and determine the source of the changes via radiation interactions in the composite's constituent materials. The MWNT nanocomposite was irradiated to a fluence of 1.5×10^{14} 1 MeV (Si-eq) neutrons and the damage to the nanocomposite was investigated with tensile strength and EMI-SE measurements to observe the gross change to the composite. Additionally, Raman spectroscopy was applied in an attempt to attribute the changes in the composite to radiation damage in either the polymer, the MWNTs, or both.

The tensile strength and the Young's Modulus both had increases, 6% and 10% respectively, due to neutron irradiation. The increases, while measureable, are insignificant in terms of design. While displacement damage to the MWNTs reduces the strength of the individual nanotubes, the nanocomposite was designed such that the MWNT plies provide little structural integrity to the composite. Therefore, it was not expected for the damage to the MWNT layers to cause any significant weakening of the composite overall. The woven E-glass and polymer layers are the main source of structure in the composite.

Both the MWNT plies and the E-glass layers, however, contain the same polymer, bismaleimide. Neutron irradiation leads to displacement damage in the polymer matrix. This damage breaks the original polymer bonds and leads to either scission or cross-linking of the polymer chains. Epoxy resins, such as bismaleimide, are known to cross-link following radiation damage. A known result of cross-linking in polymers is increased strength. This is a result of the additional bonds formed during cross-linking. The breaking of the original bonds shortens the cross-linked polymer chains, however, reducing the polymer ductility, or increasing the brittleness of the polymer. The effects of the neutron irradiation on the polymer matrix are responsible for the increase in tensile strength and Young's Modulus.

The EMI-SE of the nanocomposite increased slightly for short periods after irradiation, and then annealed back to the pre-irradiation conditions within 264 hours. The fact that the material does not degrade with neutron irradiation suggests that the composite can be used for electromagnetic shielding. The MWNT plies showed no sign of degradation in terms of EMI-SE during or after the irradiation. While these layers are insignificant in terms of the tensile strength, the layers enhance the composite's conductivity, directly increasing the EMI-SE. Previous work [3] showed that a fiberglass control sample provided only -0.7 dB of EMI-SE. Therefore, the two plies of MWNTs provided an average of -23.8 dB of shielding effectiveness, despite the small contribution it made to the composite size overall. The reduction over time in EMI-SE after irradiation suggests that there is some damage other than the displacement damage to the MWNTs affecting the conductivity of the sample. The polymer is known to cross link as a result of neutron irradiation. If the polymer is conductive, and the damage anneals over

time, then this could explain the return to pre-irradiation values of EMI-SE. This would indicate that the cross-linking in the MWNTs is not as significant to the increase in conductivity.

The Raman study showed that neutron irradiation did cause quantifiable damage to the MWNTs plies. Before irradiation, the average D/G ratio of the sample was 0.19. Following the neutron irradiation at a fluence of 1.5×10^{14} 1 MeV (Si-eq) neutrons/cm², the average D/G ratio was 0.48. This represents a 153% increase in the D/G ratio of the MWNT ply sample. An attempt was made to quantify this result based upon assumed values of energy deposition and the density and thickness of the MWNT plies. However, without quantification of the pre-irradiation defect density and the effect of those defects on the strength of the Raman D peak, it was not possible to directly correlate neutron non-ionizing energy loss to the measured changes in Raman spectral parameters.

The nanocomposite sample did not provide the same quality of Raman data as the MWNT ply sample. An overall sample D/G ratio could not be determined due to the fluctuating background and low signal-to-noise ratio. Only a few select spots were able to be analyzed, and the results indicate that there was not as much damage in the nanocomposite sample. The average D/G ratios were 0.62 and 0.58 before and after irradiation, respectively. The error was ± 0.1 , so the averages are both within the error of the calculation. Hence the results for the nanocomposite sample turned out to be inconclusive. While the data shows no measureable increase in damage, it does not mean the sample was not damaged by neutrons.

After further investigation of the experimental techniques, it is believed that the high background noise is caused by a combination of the rough surface of the

nanocomposite in conjunction with luminescence caused by the polymer on the surface of the sample. The surface, with changes in height up to 130 nm, makes it difficult for the autotrack feature to focus at each step. Additionally, the luminescence affects the laser signal that is returned to the system, giving a large background reading in the spectra.

In another measurement of the nanocomposite sample, it was found that for the best results, a depth profile needed to be made at each location where data would be measured. The depth profile allowed the researcher to determine the optimum focal point at which the data should be collected for each location. This allowed for the best results for each data location, but requires the system to manually reset each time. Unfortunately, this method was not used for data collection, and priorities and competing research did not allow for another set of measurements on the available Raman spectroscopy system.

6.2 Recommendations for Future Research

The initial plan for this research was to use a much higher fluence (1-2 orders of magnitude higher), for electron irradiation than previous researchers. Due to competing priorities of research and maintenance issues with the electron accelerator, the electron irradiation to a target fluence of $10^{18} \text{ e}^-/\text{cm}^2$ did not occur. It is recommended that electron irradiation be a priority for future research on this material and/or other similar nanocomposite materials.

The first recommendation is to include a control sample for comparison, as was done in previous research [3]. A MWNT ply sample was created for the Raman spectra study, but the only sample available for comparison was the nanocomposite. One of the

objectives of this research was to quantify the difference in radiation damage to the MWNTs and the polymer. This proved to be a difficult task as the Raman data for the nanocomposite was inconclusive. If a control sample was made without MWNTs, then the Raman spectra of this sample before and after irradiation could have been compared to the MWNT ply and nanocomposite measurements. This may have provided more conclusive data in terms of quantifying the differences.

The tensile strength testing was fairly straightforward and went according to the experimental plan. For future research, it is recommended that there be additional samples irradiated so that the tensile testing can be conducted similar to the EMI-SE testing, where the tests were conducted over time to observe the effects of annealing on the material. If the cross linking in the polymer did anneal over time, it needs to be assessed as to its effect on the tensile strength. The use of control samples for tensile testing would make this possible. While the bulk of the tensile strength is provided by the E-glass layers, it would have been interesting to compare the change in tensile strength of the nanocomposite to that of a control sample to see if the MWNTs provided any additional structural support to the E-glass.

A new method for quantifying the damage to the polymer needs to be investigated. Raman spectroscopy relies on the crystal structure of the MWNTs to provide the signal for the spectra. The amorphous nature of the polymer does not produce a clearly defined Raman spectrum that is useful in analyzing damage levels as is true for MWNT. It is recommended that other methods, such as Atomic Force Microscopy or Electron Paramagnetic Resonance, be investigated for use in delineating the effects to the polymer.

The nanocomposite Raman spectroscopy measurements need to be made manually using a depth profile at each location to determine the optimum depth at which to collect the data. This cannot be done by the system automatically, so it will be more time and labor intensive. It is recommended to make a smaller map, either a line or grid map of 20-30 data points, using a depth profile to determine the optimum focal point for each measurement.

Appendix A

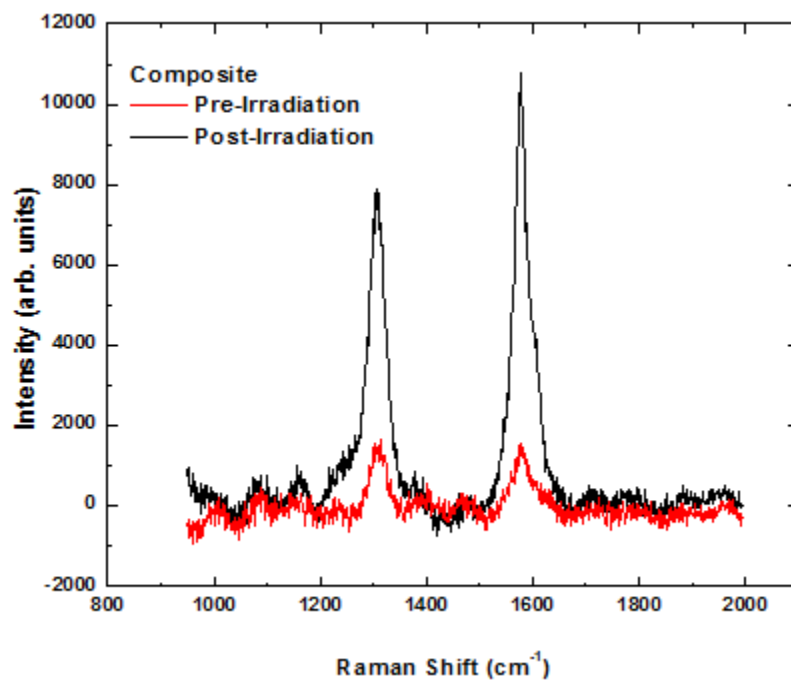


Figure 37. The Raman spectra of the nanocomposite sample. The red curve represents the pre-irradiation spectra and the black curve represents the post-irradiation curve. There appears to be a large change caused by radiation, but the intensities are not normalized.

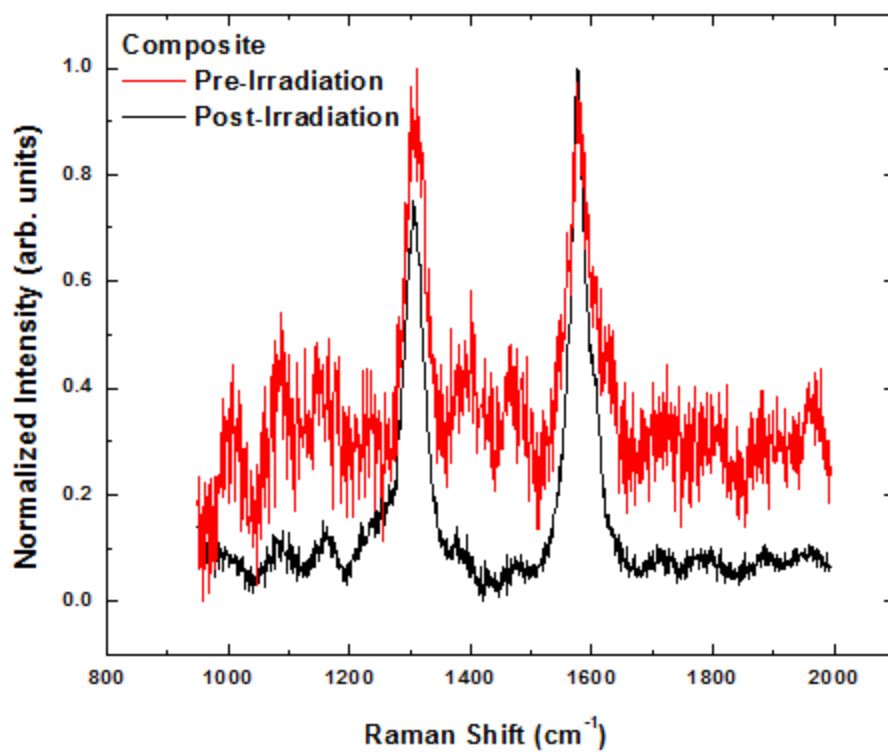


Figure 38. The Raman spectra of the nanocomposite sample. The red curve represents the pre-irradiation spectra and the black curve represents the post-irradiation curve. The peak intensities have been normalized and the data now appears to be inconclusive.

BIBLIOGRAPHY

- [1] J. Sellers, *Understanding Space: An Introduction to Astronautics*, New York: The McGraw-Hill Companies, 1994.
- [2] "Cosmic Rays," NASA, 2Feb 2010. [Online]. Available: <http://imagine.gsfc.nasa.gov> [Accessed 7 12 2012].
- [3] Q. H. T. Lu, "Durability of MWCNT Composites Under Electron and Neutron Irradiation.", Air Force Institute of Technology, Wright Patterson AFB, OH, 2012.
- [4] K. Chong, "Evaluation of Nanocomposite for Shielding Electromagnetic Interference.", Air Force Institute of Technology, Wright Patterson AFB, OH, 2011.
- [5] B. T. Harder, "Evaluation of nanocomposites as Lightweight Electronic Enclosures for Satellites' Applications.", Air Force Institute of Technology, Wright Patterson AFB, OH, 2008.
- [6] N. A. Duncan, "Changes to Electrical Conductivity in Irradiated Carbon Nanocomposites," Air Force Institute of Technology, Wright Patterson AFB, OH, 2011.
- [7] MIL-STD-1809. *Space Environment for USAF Space Vehicles*, United States Air Force, 1991.
- [8] T. Berger, "The Space Radiation Environment, A Brief Review," 2001. [Online]. Available: <http://www.ati.ac.at/~vanaweb/spacerad.html>. [Accessed 7 12 2012].
- [9] M. Piggott, "Interface Properties and Their Influence on Fiber Reinforced Polymers," in *Composite Applications: The Role of Matrix, Fiber, and Interface*, New York, VCH, 1992.
- [10] M. Monthioux and V. Kuznetsov, "Who Should be Given the Credit for the Discovery of Carbon Nanotubes?", *Carbon*, vol. 44, no. 9, pp. 1621-1623, 19 March 2006.
- [11] S. Gullapalli and M. Wong, "Nanotechnology: A Guide to Nano-Objects", *Chemical Engineering Progress*, vol. 107, no. 5, pp. 28-32, 2011.

- [12] S. Reich, C. Thomsen, and J. Maultzsch, *Carbon Nanotubes*, Weinheim: Wiley-VCH, 2004.
- [13] M. Yu, O. Lourie, M. Dyer, K. Moloni, T. Kelly, and R. Ruoff, “Strength and Breaking Mechanism of Multiwalled Carbon Nanotubes Under Tensile Load,” *Science*, vol.287, no. 5453, pp. 637-640, 2000.
- [14] A. Rochefort, “Nanotechnology Now”, 2013. [Online]. Available: <http://www.nanotech-now.com/nanotube-buckyball-sites.htm>. [Accessed 5 12 2012].
- [15] M. Dresselhaus, G. Dresselhaus, R. Saito, and A. Jorio, “Raman Spectroscopy of carbon nanotubes”, Elsevier, *Physics Reports*, vol. 409, pp. 47-99, 2005.
- [16] S. Belluci, “Carbon Nanotubes: Physics and Applications”, *Physics Status Solidi*, vol. 2, no. 1, pp34-47, 2005.
- [17] S. Yellampalli, *Carbon Nanotubes –Synthesis, Characterization, Applications*, InTech, 2011.
- [18] “Carbon Nanotubes: Graphene on a Roll”, Partnership for Research and Education in Materials, 2008. [Online] Available: <http://academic.pgcc.edu/~ssinex/nanotubes/>. [Accessed 8 11 2012].
- [19] J. McGary, “Electrostatic Discharge Properties of Irradiated Nanocomposites”, Air Force Institute of Technology, Wright Patterson AFB, OH, 2009.
- [20] D. Coy, “Changes to Electrical Conductivity in Irradiated Carbo-Nickel Nanocomposites”, Air Force Institute of Technology, Wright Patterson AFB, OH, 2010.
- [21] “Emi Shielding Theory”, Spira Manufacturing Corporation, 2012. [Online]. Available: http://www.spira_emi.com/theory.htm. [Accessed 14 11 2012].
- [22] “Shielding Theory”, Learn EMC, 2012. [Online] Available: http://www.learnemc.com/tutorials/Shielding01/Shielding_Theory.html. [Accessed 14 11 2012].
- [23] C. Paul, *Introduction to Electromagnetic Compatibility*, New York: Wiley & Sons, Inc., 2006.
- [24] N. A. Dowling, *Mechanical Behavior of Materials*, 2nd Edition, Upper Saddle River: Prentice- Hall, Inc., 1999.

- [25] C. Luebkehan, "University of Oregon Lecture", 2012 [Online]. Available: http://pages.uoregon.edu/struct/courseware/461/461_lecture24/461_lecture24.html. [Accessed 4 12 2012].
- [26] D. Rees, *Basic Engineering Plasticity – an Introduction with engineering and Manufacturing Applications*, Waltham: Butterworth-Heinemann, 2006.
- [27] E. Smith and G. Dent, *Modern Raman Spectroscopy - A Practical Approach*, West Sussex: Wiley, 2005.
- [28] D. Gardiner and P. Graves, *Practical Raman Spectroscopy*, Berlin: Springer-Verlag, 1989.
- [29] J. Best, "Materials Characterization of Bundled Single Wall Carbon Field Effect Transistors on Silicon Oxide Substrate", Poster Presentation, Air Force Institute of Technology, Wright Patterson AFB, OH, 2012.
- [30] Z. Ni, "Defects in Graphene: A Raman Spectrographic Investigation", Department of Physics, Southeast University, Nanjing, China, 2010.
- [31] P. Rinard, "Neutron Interactions with Matter", American Federation of Scientists, 1991, pp. 357-377.
- [32] A. Holmes-Siedle and L. Adams, *Handbook of Radiation Effects*, 2nd Edition, New York: Oxford University Press, 1993.
- [33] "32 Defects in Solids", concimientos.com.ve, 24 June 2010. [Online]. Available: <http://conocimientosdefectosinsolids.blogspot.com/2010/06/frenkel-defect-and-wigner-effect.html>. [Accessed 3 12 2012].
- [34] A.V. Krasheninnikov and K. Nordlund, "Irradiation Effects in Carbon Nanotubes", Elsevier, vol. Nuclear Instruments and Methods in Physics Research B, no. 216, pp. 355-366, 2004.
- [35] T. Gray, "Investigation of Gate Current in Neutron Irradiated AlGaN/GaN Heterogeneous Field Effect Transistors Using Voltage and Temperature Dependence", Air Force Institute of Technology, Wright Patterson AFB, OH, 2007.
- [36] I. Aitken and K. Ralph, "Some Effects of Radiation in Cast Epoxide Resin Systems," AERE-R, vol. 3085, 1960.

- [37] R.G. Sonkawade, V. Kumar, S. Annapoorni, S.G. Vaijapurkar, and A.S. Dhaliwal, “Effects Of Gamma Ray And Neutron Radiation On Polyaniline Conducting Polymer”, Indian Journal of Pure & Applied Physics, vol. 48, pp. 453-456, July, 2010.
- [38] D.B. Mawhinney, V. Naumenko, A. Kuznetsova, J. Lui, and R. Smalley, “Surface Defect Site Density On Single Walled Carbon Nanotubes By Titration”, Elsevier, vol. 324, pp. 213-216, 2000.
- [39] F. Cataldo, “ A Raman Study On Radiation-Damaged Graphite By Gamma-Rays”, Carbon, vol. 38, pp. 623-641, 1999.
- [40] “Space Weather Effects On Satellites,” [Online]. Available: <http://www.spaceweather.gc.ca>. [Accessed 7 12 2012].
- [41] E. Skulason, Novemeber 2005. [Online]. Available: <https://notendur.hi.is/~egillsk/stuff/annad/Egill.Slides2.pdf>. [Accessed 7 11 2012].

REPORT DOCUMENTATION PAGE				Form Approved OMB No. 074-0188	
<p>The public reporting burden for this collection of information is estimated to average 1 hour per response, including the time for reviewing instructions, searching existing data sources, gathering and maintaining the data needed, and completing and reviewing the collection of information. Send comments regarding this burden estimate or any other aspect of the collection of information, including suggestions for reducing this burden to Department of Defense, Washington Headquarters Services, Directorate for Information Operations and Reports (0704-0188), 1215 Jefferson Davis Highway, Suite 1204, Arlington, VA 22202-4302. Respondents should be aware that notwithstanding any other provision of law, no person shall be subject to any penalty for failing to comply with a collection of information if it does not display a currently valid OMB control number.</p> <p>PLEASE DO NOT RETURN YOUR FORM TO THE ABOVE ADDRESS.</p>					
1. REPORT DATE (DD-MM-YYYY) 21 03 2013		2. REPORT TYPE Master's Thesis		3. DATES COVERED (From - To) June 2011 - Mar 2013	
4. TITLE AND SUBTITLE Changes to Tensile Strength and Electromagnetic Shielding Effectiveness in Neutron Irradiated Carbon Nanocomposites				5a. CONTRACT NUMBER	
				5b. GRANT NUMBER	
				5c. PROGRAM ELEMENT NUMBER	
6. AUTHOR(S) Shinn, James F., Major, USA				5d. PROJECT NUMBER	
				5e. TASK NUMBER	
				5f. WORK UNIT NUMBER	
7. PERFORMING ORGANIZATION NAME(S) AND ADDRESS(S) Air Force Institute of Technology Graduate School of Engineering and Management (AFIT/ENV) 2950 Hobson Way, Building 640 WPAFB OH 45433-8865				8. PERFORMING ORGANIZATION REPORT NUMBER AFIT-ENP-13-M-32	
9. SPONSORING/MONITORING AGENCY NAME(S) AND ADDRESS(ES) Air Force Research Laboratory Max D. Alexander 2941 Hobson Way Wright Patterson, OH 45433-7750 (937)785-9135 max.alexander@wpafb.af.mil				10. SPONSOR/MONITOR'S ACRONYM(S) USAF AFMC AFRL	
				11. SPONSOR/MONITOR'S REPORT NUMBER(S)	
12. DISTRIBUTION/AVAILABILITY STATEMENT APPROVED FOR PUBLIC RELEASE; DISTRIBUTION UNLIMITED.					
13. SUPPLEMENTARY NOTES					
14. ABSTRACT Electromagnetic interference shielding effectiveness (EMI-SE) and tensile strength of nanocomposites containing multi-walled carbon nanotubes (MWNTs) are investigated following neutron irradiation. This nanocomposite material consists of two plies of MWNTs in an epoxy resin, and 4 plies of an E-glass substrate. EMI-SE measurements over the X-band frequency spectrum and monotonic tension tests to determine Young's Modulus were performed before and after irradiation on the nanocomposite material. The nanocomposite and the MWNT plies were irradiated to a total fluence of 1.4×10^{14} 1 MeV (Si-eq) n/cm ² . The nanocomposites showed an average increase of 8 dB in shielding effectiveness after irradiation. However, the increase was not permanent with a return to pre-irradiation values after approximately 10 days at ambient temperature and pressure. The tensile strength and Young's Modulus showed an 8% and 10% increase, respectively, following irradiation. This small increase is a result of the neutron induced embrittlement of the nanocomposite. Raman spectra of the MWNT plies showed a 150% increase in the D/G peak ratios after irradiation. This indicates damage in the plies due to neutron interactions in the MWNTs that does not lead to a commensurate reduction in EMI-SE or tensile strength in the nanocomposite material.					
15. SUBJECT TERMS Nanocomposite, radiation effects, neutron irradiation, Raman spectroscopy					
16. SECURITY CLASSIFICATION OF:			17. LIMITATION OF ABSTRACT	18. NUMBER OF PAGES	19a. NAME OF RESPONSIBLE PERSON
a. REPORT	b. ABSTRACT	c. THIS PAGE			John McClory, Ph.D, AFIT/ENP
U	U	U	UU	91	19b. TELEPHONE NUMBER (Include area code) (937) 255-6565, ext 7308 (john.mcclory@afit.edu)

Standard Form 298 (Rev. 8-98)
Prescribed by ANSI Std. Z39-18